Structural and Kinetic Studies of Structure I Gas Hydrates via Neutron Powder Diffraction and Low Temperature X-Ray Diffraction

A Dissertation Presented for the
Doctor of Philosophy
Degree
The University of Tennessee, Knoxville

Susan Michelle Everett
May 2013

DEDICATION

I dedicate this work to my husband Chris (babers).
He kept saying, “You can do this! I’ll support you however I need!”
He has surprising patience when it comes to my crazy.
I love that man.

To my mom and dad, who raised me to be independent,
do things the right way and take pride in my work.
They’ve never stopped loving and nurturing me in all my 40 years.
Mom always knew that
I asked too many questions not to be a scientist,
and my dad, says he is still living just to see me walk across that stage.

And to my close friends, Toby and Christine, who kept asking questions
and cheering appropriately, even though their eyes glazed over
when the nerdy details came out. If they could have used their collective writing
skills to save me, they would have.

Of course enough cannot be said about the influence Claudia had on this
adventure. Without her constant search for worthy students to send running
head first into science, this experience would not have been possible. Her zeal
for understanding and quest for scientific discovery is unparalleled.
Not to mention her cheerleading skills, if not for those,
I most definitely would have lost this game.

ACKNOWLEDGEMENTS

This work is supported by National Science Foundation Grant No. DGE0801470, "Sustainable Technology through Advanced Interdisciplinary Research" (STAIR), awarded to the University of Tennessee, Knoxville. Also in small part by the Office of Fossil Energy through Field Work Proposal FEAB111 "Hydrate Formation and Dissociation in Simulated and Field Samples."

Neutron powder diffraction data were collected at the Spallation Neutron Source and the High Flux Isotope Reactor. Low temperature x-ray powder diffraction data were collected at the Center for Nanophase Materials Sciences. All of these are sponsored at Oak Ridge National Laboratory by the Scientific User Facilities Division, Office of Basic Energy Sciences, U.S. Department of Energy.

The experiences I shared with the STAIR community were invaluable. I am thankful I was a part of such a talented and diverse group. I would especially like to acknowledge and thank David Keffer and Jane Breder. David was involved with my research from the beginning and was a valuable asset to my development. Jane was a proud mother hen, and I am glad she was there for me.

There have been a number of people along the way that has made this journey come to a successful end. The scientific community that I was a part of at ORNL supported me, and gave me every tool they could to make me successful. Also, my fellow graduate students, without their commiseration I would have felt completely alone in the world.

ABSTRACT

Gas hydrates are materials of interest as sources for clean energy, carbon sequestration, greenhouse gas mitigation, and gas storage. This body of work presents two projects that each separately explore one aspect of the potential found in gas hydrates. Chapter 1 tackles the structural changes found to occur over the CO_2 [carbon dioxide] - CH_4 [methane] hydrate solid solution. The application here pertains to the sequestration of CO_2 in natural gas hydrates found in permafrost regions and ocean floors. As CO_2 is injected into the hydrate reservoir, CH_4 is released and recovered for energy use. Samples synthesized from liquid water were studied using high-resolution neutron diffraction. Static images of the nuclear scattering density of the free moving gas molecules were determined. Cage occupants and occupancies, the volume change of the unit cell and the individual cages based on composition were determined. Chapter 2 pertains to the decomposition of methane hydrate and a phenomenon termed anomalous preservation. Three samples were studied using *in situ* low temperature x-ray diffraction as they decomposed over a temperature range of 140 – 260 K and the kinetics were analyzed using the Avrami model. Activation energies and Avrami constants were determined for two temperature ranges within the overall range.

TABLE OF CONTENTS

INTRODUCTION 1
Gas Hydrates 1
Energy Source 3
Global Climate Change 5
Gas Storage 7
EXPERIMENTAL METHODS 9
Sample Synthesis 9
X-Ray Diffraction 11
Neutron Diffraction 14
Rietveld Refinements 16
CHAPTER I Molecular Visualization of CH_4 – CO_2 Solid Solution in Gas Hydrates via High-resolution Neutron Powder Diffraction 22
Abstract 23
Background 23
Experimental 25
Results and Discussion 27
Conclusion 31
CHAPTER II Kinetic Studies OF Methane Hydrate Decomposition via Low Temperature X-ray Powder Diffraction 33
Abstract 34
Background 34
Experimental 38
Results and Discussion 39
Conclusion 44
CONCLUSION 46
Results 46
Applications and Future Studies 48
LIST OF REFERENCES 50
APPENDIX 59
Figures 60
Tables 89
VITA 93

LIST OF TABLES

Table A - 1. Experimental results 89
Table A - 2. Rietveld results 90
Table A - 3. Cage occupancies and occupants 91
Table A - 4. Avrami constants 92

LIST OF FIGURES

Figure A - 1. Pipeline hydrate plug 60
Figure A - 2. Cage structures for gas hydrates 61
Figure A - 3. Hydrate guest size 62
Figure A - 4. CO_2 hydrate phase diagram 63
Figure A - 5. CH_4 hydrate phase diagram 64
Figure A - 6. Energy reserves 65
Figure A - 7. Global hydrate deposits 66
Figure A - 8. Hydrate reserve estimates 67
Figure A - 9. Experimental aids 68
Figure A - 10. Parr vessel 69
Figure A - 11. McHugh cell 70
Figure A - 12. Hydrate dissociation 71
Figure A - 13. Diffraction of x-rays by atomic planes 72
Figure A - 14. LTXRD environmental chamber 73
Figure A - 15. V can 74
Figure A - 16. POWGEN detector bank 75
Figure A - 17. Cross section comparison 76
Figure A - 18. Large and small cage of sI placed in the unit cell 77
Figure A - 19. Powder pattern for 50% CH_4 nominal sample 78
Figure A - 20. Nuclear scattering densities 79
Figure A - 21. Experimental vs. CSMHYD predicted occupancy results 80
Figure A - 22. Lattice parameters, ADPs, cell volumes, and density 81
Figure A - 23. Density of mixed hydrates 82
Figure A - 24. Temperature dependent decomposition 83
Figure A - 25. Waterfall plot of isothermal decomposition at 250K 84
Figure A - 26. Avrami plots for Region 2 85
Figure A - 27. Avrami plots for Region 3 86
Figure A - 28. Arrhenius plot for region 2 87
Figure A - 29. Arrhenius plot for region 3 88

INTRODUCTION

Gas Hydrates

Gas hydrates, also referred to as clathrate hydrates, are nonstoichiometric crystalline water inclusion compounds wherein the water host lattice is a hydrogen-bonded network that traps small gas molecules, approximately 9 Å or less (Koh and Sloan 2007) inside cages. High pressure (2 − 1,000 MPa) and/or low temperature (<323 K) are required for hydrate formation and stability (Sloan 2003). There are three primary hydrate structures; the structure formed is dependant on the type of gas molecule stored inside and the pressure conditions under which it was formed. They readily occur in nature; found in permafrost regions and in sediments of the continental margins.

Evidence of the discovery of hydrates may date back to 1778 when Priestly observed a material from freezing H_2O and SO_2 (Sloan and Koh 2008). However, there is not enough documentation to substantiate the claim. The first well-documented discovery is attributed to Sir Humphry Davy in 1810. He observed the production of a solid material from liquid H_2O and Cl gas (oxymuriatic gas) above the freezing point for water (Davy 1811). Hydrates went without consideration until Hammerschmidt from Canada in 1934 discovered that hydrates were the reason gas lines were blocked (Figure A - 1 (all Tables and Figures are in the Appendix)) in high-pressure low temperature conditions offshore and onshore. Since then, flow assurance has been a top priority for the oil/gas industry (Koh, Sloan et al. 2011). It was not until 1964 in Russia that the first permafrost natural gas hydrate (NGH) was discovered and later marine hydrates were found in the 1970's (Demirbas 2010). NGH is formed from either biogenic or thermogenic methane sources. The current state of hydrates is no longer in the discovery stage, but rather in the exploitation stage.

The three primary structures are known as structure I (sI), structure II (sII), and structure H (sH). They are denoted by the shape and number of the faces that make up the cage; A^xB^y where A and B are the number of sides of each face, and x and y are the numbers of faces that make up each cage (Figure A - 2). sI has two small cages (5^{12}) and six large cages ($5^{12}6^2$) made from 46 H_2O molecules per unit cell. sII has sixteen small cages (5^{12}) and eight large cages ($5^{12}6^4$) made from 136 H_2O molecules per unit cell. Both sI and sII crystallize in the cubic crystal system with lattice parameters of approximately 12 and 17 Å, respectively. sH has three (5^{12}), two ($4^35^66^3$) and one ($5^{12}6^8$) from 34 H_2O molecules, and crystallizes in the hexagonal crystal system. Although the structures are different in cage size and number, they are all 85 mol% water and 15 mol% guest (Sloan 2003).

The most influential factor in structure type is the guest molecule size (Figure A - 3). Most naturally occurring hydrates are sI comprised of small guests in the range of 4 − 5.5 Å (Sloan 2003). Larger molecules of 6 − 7 Å and very small molecules <4 Å usually crystallize as sII and are generally found in synthetic hydrates, however they have been found in nature as well. sH can be found in either natural or unnatural samples with a mix of small and large molecules, but are rare. Two gases that form sI separately may form sII when mixed, if the small molecule is so small that it is on the edge of sI formation and the large molecule is so large that it is on the other end of sI formation (Ripmeester 2000; Hester and Sloan 2005). For example, gas hydrates in oil pipelines are mainly sII due to the fact that the methane rich gas found with oil also contains propane and isobutene (Koh, Sum et al. 2010). Most clathrate hydrates found in ocean sediments and under permafrost are sI because that methane has very little large hydrocarbons in accompaniment.

It is not required for 100% of the cages in a structure to be full. In fact they are known has nonstoichiometric because they are not always fully occupied (Koh, Sloan et al. 2011). However, the structure in not stable unless a critical number is filled. For the most part there is only one gas molecule per

cage. The exception comes from high-pressure hydrates such as hydrogen, where two molecules can be found in the small cage and up to four in the large cage.

Nucleation, crystallization, growth, and agglomeration are all important parts of hydrate formation (Demirbas 2010). Nucleation propagates from the gas-water interface after gas has dissolved into the water, indicating gas rich conditions are required. PVT effects govern the rate of formation as well as both mass and heat transfer. Mass transfer dominates in the gas supply regime. Gas has to dissolve in the liquid and then be moved close into the crystal for a constant supply of gas rich solution. Hydrate formation is an exothermic process requiring heat to be moved way from the growing crystals. Therefore hydrate formation is dependent on reaction, transport and PVT effects.

Since gas hydrates require low temperature and high pressure, the phase diagrams can be somewhat complicated. The mixed CO_2/CH_4 system is not well published, but each end member has been explored in detail. Figure A - 4 and Figure A - 5 are phase diagrams for CO_2 and CH_4 hydrate respectively. The phase diagrams can be complicated and show that these are complex systems.

Energy Source

The amount of hydrocarbons (mostly methane) stored in NGH at the very minimum is approximated to be twice the amount of all other fossil fuel reserves combined (Figure A - 6). The US uses about 23 trillion ft^3 (tcf) per year. Modest calculations estimate there is 700,000 tcf of gas stored in NGH, although the estimates in amount have changed drastically over the years. Milkov, Archer et al., and Klauda et al. report values ranging from 500 to 74,400 Gt (Milkov 2004; Klauda and Sandler 2005; Archer, Buffett et al. 2009). While Collett et al. reports thermogenic hydrate reserves in the Gulf of Mexico alone could range fro 5 to 500 Gt (Collett and Kuuskraa 1998). However, the vast majority of hydrated gas is in ocean sediments and is the result of biogenic sources. Over 230 NGH

reservoirs have been identified (Figure A - 7) worldwide in 79 countries (Sun, Li et al. 2011).

Like other natural resources, there are varying types of deposits with varying degrees of accessibility. Higher concentrations of gas were thought to be recoverable from permafrost regions rather than marine sources due to the terrestrial matrix. The most easily recoverable resources are within sand deposits, as found in the Arctic (Moridis and Sloan 2007). The concentration in these sand deposits is very high, 60 − 90% of the pore space, compared to unconsolidated or undeformed muds at 10% pore filling (Boswell 2009), which are found in the ocean (Figure A - 8). However, in 1999 Japanese explorers discovered a large marine hydrate deposit in sand off the southeastern shore of Japan. In 2009 a drilling expedition in the Gulf of Mexico confirmed 2 of 3 hydrate reservoirs to be contained in sand. It is now estimated that the in-place resources (tcf) are made up of 100's in Arctic sand reserves, 1000's in marine sands and 100,000's in muds (Boswell and Collett 2006). Arthur Johnson, a retired geologist of the oil industry now in energy consultation in Louisiana, stated at a workshop on methane hydrates in Vienna that he predicts NGH will become 10 − 15% of the natural gas feedstock within the next two decades (Bohannon 2008).

In 2002 the first attempts to recover gas from NGH were launched in the Arctic of Canada known as the Mallik project (Kerr 2004). It was a collaboration of six countries led by Japan and Canada. The scale was very small, but proved that gas could be produced from hydrates. In Nankai, Japan in 2004 large scale drilling projects began (Demirbas 2010). Due to a lack of resources in Japan the country is forced to import 99% of the gas and oil it consumes (Kerr 2004). Recovery from gas hydrates offers Japan a domestic source of natural gas, resulting in the goal of gas production from hydrates by 2015 (Bohannon 2008). India began offshore drilling in several sites in 2006.

Four things are needed for hydrate formation: gas, water, high pressure and low temperature. Recovering methane from natural deposits requires

changing one of these things. Lowering the pressure, disrupting the hydrogen bonds by adding energy, or adding hydrogen-bonding chemicals in order to disturb the hydrate structure are all approaches explored to recover methane from NGH. With the exception of the hydrate formations often distributed within sediments there are not many technical roadblocks to extracting natural gas from hydrate deposits. However, the environmental impact of that process needs serious consideration (Koh, Sloan et al. 2011).

Global Climate Change

Gas concentrations in the atmosphere are the driving force behind our climate (Kroeger, di Primio et al. 2011). Gases termed greenhouse gases act as a blanket to hold in radiative energy from the earth. The most noted is CO_2, specifically from anthropogenic sources. CH_4 is also a greenhouse gas and said to be 20 times more effective in irradiative heat generation than CO_2 (Rasmussen and Khalil 1981), and it makes up 15% of the present warming trend (Hatzikiriakos and Englezos 1993). There is evidence that CH_4 levels have doubled between 1960 and 2000 representing a six-fold increase over any previous 40 year period in the last two millennia (Kroeger, di Primio et al. 2011). The increase in methane over the last few decades is anthropogenic due to food and fertilizer production, and overall there has been a carbon increase in the industrial age due to fossil fuel fed power plants. The recent increase of anthropogenic carbon in the atmosphere closely resembles an excursion 55 million years ago, which began the Paleocene Eocene Thermal Maximum. This event has been linked to a methane release of catastrophic proportions from NGH (Kennett and Stott 1991; Dickens, Oneil et al. 1995; Thomas, Zachos et al. 2002).

As the climate changes, NGH reservoirs are in danger of disruption. As mentioned earlier, a change in temperature or pressure will disrupt the hydrate stability zone. The solid will decompose into water and gas,

$$CH_4 \bullet 5.75H_2O \rightarrow H_2O\ (\ell) + CH_4\ (g)$$

This can be accomplished by overall temperature increase, ice sheets retreating or sea level decrease. In deep water hydrates the decomposition would be from bottom up, and in shallow water hydrates, from top down (Kroeger, di Primio et al. 2011). The Arctic Ocean will be the most affected, as the models show the biggest increase in temperature will be there. The Arctic permafrost regions have already begun to decompose (Kvenvolden 1988; Kvenvolden 1988); however the amount released has not shown a substantial effect. The 1 °C increase in ocean temperature over the last 30 years has caused an estimated 20 Tg/year release of CH_4 in the Svalbard Archipelago (Westbrook, Thatcher et al. 2009). Davy et al. reported some 10,000 gas releases east of New Zealand where some released as much as several Tg (Davy, Pecher et al. 2010). If temperatures continue to rise, hydrate dissociation could result in a "run-away" greenhouse effect (Hatzikiriakos and Englezos 1993). Current rising temperature trends point to temperatures in hydrate zones beginning to rise in ~100 yrs. There is evidence that hydrate dissociation from an increase in water temperature has resulted in catastrophic landslides at continental margins (Paull, Ussler et al. 1991; Nisbet 2002; Davy, Pecher et al. 2010). In turn this causes the release of large amounts of methane from both the hydrate structure and free gas trapped below the hydrate reservoirs. This brings up the question as to whether that methane makes it to the atmosphere.

The argument arises from the fact that methane can be turned into CO_2 through oxidation before entering the atmosphere, dissolved into the seawater (Kroeger, di Primio et al. 2011), or sequestered in carbonates (Boetius and Suess 2004). However, if the seawater depth were shallow, there would not be enough time for oxidation, and if the concentration of CH_4 in the water is already high, no additional CH_4 could be dissolved. The solubility of CH_4 in seawater is dependent on water specifics (e.g. chemical composition, temperature, etc.). In the Santa Barbara Channel, California, at a depth of 20 − 70 m, 50% of the

released CH_4 breeches the surface (Kvenvolden and Harbaugh 1983). In stratified oceans such as the Black Sea, as little as 1.5% is released from the water (Schmale, Greinert et al. 2005). In total, Kvenvolden et al. reported that about 2/5 of CH_4 seepage enters the atmosphere (Kvenvolden, Lorenson et al. 2001). Part of that is caused from masses of hydrate deposits that are freed and float into the upper 100 m of the ocean.

Both CO_2 and CH_4 hydrate form as sI; however, CO_2 hydrate is more thermodynamically stable than CH_4 hydrate. These facts make it a promising venture to replace CH_4 in NGH with CO_2. It mitigates the spontaneous release of CH_4, recovers it for energy use, and sequesters CO_2 all at once. As found in natural formations, hydrate structures are separated from the mineral matrix by a liquid buffer (Kvamme, Graue et al. 2007), which allows for the injection of CO_2 and the escape of CH_4.

Mining methods explored thus far for methane extraction include the addition of hydrate inhibitors (Gayet, Dicharry et al. 2005), depressurization of methane deposits (Ji, Ahmadi et al. 2001), and thermal stimulation (Tsimpanogiannis and Lichtner 2007). All or any of these techniques individually could destabilize the seafloor. However, the use of CO_2 could help to mitigate the destabilization by replacing the CH_4 with CO_2. In this scenario the structure may be less likely to collapse and cause catastrophic geological disasters such as earthquakes and submarine landslides (Zhao, Xu et al. 2012). It could also serve to solve some of the problems associated with current mining strategies such as in the inhibitor method, which has the potential for high cost and damage to the surroundings.

Gas Storage

The clathrate hydrate structures offer a way to compress gas into a small volume. The cages within the hydrate structures are very close together, and therefore the gas molecules are close together, much closer than in their

gaseous phase. At STP methane hydrate contains 180 volumes of gas to 1 volume of water, because of this it makes for an attractive gas storage medium (Strobel, Koh et al. 2007). In situations where there is not enough natural gas to support a liquefaction plant, the gas could be stored in hydrate pellets (Koh, Sloan et al. 2011). This process is near to commercialization for wide spread storage and transportation. The obvious benefit is a high volume percent of storage in a reversible process that only requires water.

Hydrates have also been studied as a means to store hydrogen. In the early history of gas hydrates research it was assumed that hydrogen was too small to stabilize a hydrate structure. Unlike the moderate pressures of natural hydrates, hydrogen hydrates require high pressures, more than 200 MPa at ambient temperatures (Koh, Sloan et al. 2011). They were first investigated by Dyadin et al. (Dyadin, Larionov et al. 1999) and Mao et al. (Mao, Mao et al. 2002). Mao et al. used neutron powder diffraction to characterize the hydrates and found that hydrogen occupies both the small and large cages of sII. Lokshin et al. also used neutron powder diffraction and found one molecule in the small cages and anywhere from two to four in the large cages (Lokshin, Zhao et al. 2004). The difference in cage filling was attributed to differences in temperature and pressure conditions. In the latter study it was found that the cages containing four molecules were tetrahedrally coordinated with a D_2-D_2 bond distance of 2.93 Å. This is in contrast to the 3.78 Å bond distance observed in solid hydrogen at 4 K and atmospheric pressure. Indicating that hydrates are indeed a good hydrogen storage medium with the promise of high concentration.

There are some obvious benefits to using hydrates for hydrogen storage. Both the dissociation and formation can be very fast. Hydrogen hydrate formation from bulk ice can occur in a matter of hours while formation from powdered ice can occur in a matter of minutes (Lokshin and Zhao 2006). The hydrogen is stored molecularly meaning the binding energy is so low that the generation of extra heat is not a concern (Strobel, Koh et al. 2007). The matrix is

water, which is non reactive with fuel cells, recyclable, inexpensive, and readily available.

The challenge in hydrogen storage with hydrates is the high pressure needed to stabilize hydrogen hydrate structures (200 MPa at 273 K (Dyadin, Larionov et al. 1999)). Research has shown that using helper molecules, such as THF, reduced the pressure and/or raised the temperature needed for stability. Lee et al. discovered hydrogen hydrate was stable with THF at 270 K and 15 MPa (Lee, Lee et al. 2005). This strategy results in a compromise, the addition of helper molecules helps reduce the pressure needed for formation and stability, however, these helper molecules also result in the decrease of overall hydrogen storage capacity.

EXPERIMENTAL METHODS

Sample Synthesis

Two different types of synthesis were used for these studies. The first synthesis started with hexagonal ice, I_h. Water was frozen into thin ice cubes, crushed, and sieved to a particle size of <500 μm (Figure A - 9). All preparations were performed in a liquid N_2 glove bag and/or a cold room. Once the ice was prepared, it was loaded into a 450 mL pressure vessel (Figure A - 10) with stainless steel milling media, the atmosphere was evacuated, and the vessel was pressurized with the desired gas (more specifics to follow). Gas was sent through ice-cooled coils in order to not blast the ice with room temperature gas, altering the particle size or melting the ice. This process was time consuming, and there were a number of steps that were meticulously followed for hydrate formation. The vessel containing the ice and gas was stored in a -20 °C freezer on a tumbler and rotated to promote diffusion. The black collars on the vessel shown in Figure A - 10 were designed and added specifically for use with the tumbler. The pressure was monitored until the characteristic pressure drop

associated with hydrate formation was observed to stop, at that point hydrate formation was assumed complete. This pressure drop is due to the free moving gas from the headspace being encapsulated into the closely packed cages of crystalline water. The vessel was subsequently depressurized, quenched in liquid N_2, and the resulting powders were collected into pre-cooled vials for subsequent storage in liquid N_2. Hydrate samples are stable at 77 K for some time without the help of pressure, but will not remain so indefinitely.

X-ray powder diffraction results revealed that this synthesis technique did not result in more than a 60% conversion of the ice into hydrate. I_h is well known for exhibiting preferred orientation in crystal growth. With 50% of the sample being I_h and exhibiting preferred orientation, there was an additional level of complexity to the analysis of the diffraction patterns. This synthesis method was used in chapter II of this study.

In a separate hydrates-related project, it was required for hydrate to be formed reliably on a time scale. In preparing for this project a new synthesis route was developed and used for chapter I. The synthesis was based on studies by Priest et al. (Priest, Rees et al. 2009). To perfect this synthesis method a pressure cell with sapphire windows containing gas, water, and sand was used (Figure A - 11). This pressure cell was equipped with a syringe injector for adding water. Temperature was controlled using a cooling bath where the cooling medium was allowed to flow through tubing surrounding the cell shroud, and an independent thermocouple and a pressure transducer were used to monitor the P and T conditions. This method better mimics how gas hydrates are formed in nature at the water/gas interface. Pressure was held constant by adding water to compensate for the pressure drop characteristic of hydrate formation. Figure A - 12 shows the visual progress of hydrate formation and dissociation that was tracked to ensure hydrate synthesis. Lessons learned about cooling rates and pressure from using the above method were used to modify synthesis using liquid water and pressuring with cooled gas in a 450 ml Parr vessel. Distilled water was mixed with a small amount of nucleating protein (~10

ppm) (McCallum, Riestenberg et al. 2007). Prior to pressurization with the desired gas the vessel was evacuated. After the gas was introduced the vessel was then placed in a cold room and rotated (more specifics are given in the Experimental section of chapter I). The interface between the water and gas is assumed to be where hydrate formation occurs (Sloan 2003). After the pressure drop ceases the formation is assumed to be complete, and cell and contents were allowed to warm to room temperature for 15 minutes. Subsequently the cell was placed in a freezer at -20 °C for 24 h or more. If the stainless milling media inside did not move freely when the vessel was shaken this suggested the hydrate had not formed and that the media was frozen in place by ice (I_h). If the media moved freely, it suggested hydrate formation had occurred. Subsequent X-ray and neutron powder characterization on samples synthesized using this route revealed samples with >90 wt% hydrate content.

X-Ray Diffraction

After Röntgen discovered x-rays in 1895, Max von Laue discovered x-ray diffraction in 1912, and in the same year W.L. Bragg discovered the mathematical relationship between diffraction angle and inter-atomic spacing (Stout and Jensen 1989). W.L. Bragg's father, W.H. Bragg, invented the x-ray goniometer allowing for the x-rays to be focused onto a sample enabling the atomic structure of crystalline materials to be probed with resolution on the order of nanometers. The angular position (2θ) of the diffracted beam allows for the determination of the crystal system and unit cell, while the relative intensities of the planar reflections provide information on the specifics of the atoms found in the unit cell (De Graef and McHenry 2007). For over 100 years x-ray diffraction has been a staple of many science disciplines, serving to reveal the atomic structure of a crystalline material. Due to the significance of these discoveries and their impact on science the United Nations has recognized these accomplishments by designating 2014 the International Year of Crystallography.

X-rays have wavelengths on the order of atomic spacing (0.5 − 2.5 Å (Cullity and Stock 2001)), making diffraction a desirable choice for characterizing atomic structures. The mathematics behind this are based on constructive interference and Bragg's Law. When a planar wave has a scattering event, there are two extreme possibilities for the diffracted beam (Callister 2007). One possibility is that the waves leave the scattering event and are exactly in phase with each other. When this happens, the amplitudes of the waves are additive and are said to constructively interfere with each other. On the other hand, the waves could be completely out of phase (half a wavelength off), and the amplitudes cancel each other, known as destructive interference (De Graef and McHenry 2007). When any electromagnetic wave is incident on a material, it sets in motion oscillation of the atoms. This oscillation creates spherical, concentric waves about the atoms, which will in turn begin to interact with each other. The interaction is a complex pattern of interference, where constructive interference will only occur from a specific relationship between the planar spacing and radiation wavelength (De Graef and McHenry 2007). This is known as Bragg diffraction and the resulting constructive interference is known as a Bragg peak. The fundamentals of diffraction are the same for x-ray, neutron, and electron radiation.

Figure A - 13 shows parallel planes of atoms. They are separated by a distance d_{hkl} and have the same Miller indices h, k, and l. The incoming wave represents a beam at some angle θ that is coherent, monochromatic, and parallel with wavelength λ. Atoms A and B are scattering the two rays of the beam shown and constructive interference occurs if the diffracted beam is at the same angle θ and the path length difference between the top wave and the bottom wave is an integer n wavelengths apart. This physically describes Bragg's Law. In order to satisfy the Bragg condition for constructive interference the following holds,

$$n\lambda = \overline{CB} + \overline{BD} \qquad \text{Eq. 1}$$

which can also be written,

$$n\lambda = d_{hkl}\sin\theta + d_{hkl}\sin\theta \qquad \text{Eq. 2}$$

$$n\lambda = 2d_{hkl}\sin\theta \qquad \text{Eq. 3}$$

Eq. 3 is Bragg's Law, a simple, fundamental relation to correlate inter-planar spacing and x-ray wavelength to a scattered beam's angle (Callister 2007). Destructive interference will not satisfy the Bragg condition, and intensity will be negligible compared to angles where it is satisfied.

The order of the diffracted beam is denoted by the integer n. The Bragg equation can be rewritten as

$$2\frac{d_{hkl}}{n}\sin\theta = \lambda \qquad \text{Eq. 4}$$

Then d_{hkl}/n represents inter-planar spacing for the planes ($nk\ nh\ nl$), since $d_{hkl} = 1/|g_{hkl}|$ and $n\mathrm{g}_{hkl} = nh\mathbf{a}^* + nk\mathbf{b}^* + nl\mathbf{c}^* = \mathrm{g}_{nh\ nk\ nl}$. Now n can be dropped and only first-order diffraction is considered. Even though the (100) and (200) planes may be equivalent by symmetry, they are not equivalent as $d_{100} = 2d_{200}$. Further a generalized formula expresses d_{hkl} in terms of the unit cell dimensions a, b, and c and Miller indices h, k, and l through metric tensor formalism and the Bragg equation. The equation for a cubic system, as is the case for sI and sII hydrate, is as follows:

$$d_{hkl} = \frac{a}{\sqrt{h^2 + k^2 + l^2}} \qquad \text{Eq. 5}$$

Figure A - 13 shows the most basic simple cubic arrangement where atoms are only sitting on the corners of a cubic unit cell (simple cubic). In reality the majority

of materials have more complicated structures and additional considerations must be taken into account.

Neutron Diffraction

Neutron powder diffraction (NPD) is less commonly used as a characterization method than XRD due to limited availability, access, and until recently the larger sample sizes required. The diffraction fundamentals are the same, and both XRD and NPD are useful individually and in complement. The choice of technique is often determined by what specific information is desired from the experiment. Neutrons are beneficial for hydrate characterization due to flexibility in environmental chambers, resolvability, and sensitivity to low Z elements. Neutrons are charge neutral, allowing them to penetrate deep into environmental chambers and samples (De Graef and McHenry 2007). In comparison, XRD is often thought of as a surface technique and only requires small amounts of sample. The ability of neutrons to penetrate allows for flexibility in sample environment design. Liquid N_2 temperatures (77 K) are required for working with hydrates at ambient pressure to avoid decomposition. When synthesized in the laboratory gas hydrates resemble snow. The small sample wells used in XRD are tedious to pack in liquid N_2 conditions, and the propensity of hydrate to stick to the chilled spatula makes it challenging to pack a sample holder with a smooth sample surface, which is desirable for XRD studies. The sample stage used for LTXRD in chapter II is shown in Figure A - 14. Samples for NPD are typically contained in V cans with diameters as large as 10 mm, allowing for easy sample loading. Debye-Scherrer geometry is common for neutron powder diffraction instruments, requiring the sample to be contained in a cylindrical sample holder and Figure A - 15 shows the type of can used for chapter I. Figure A - 16 shows detectors in this geometry at the POWGEN instrument, Spallation Neutron Source, Oak Ridge National Laboratory where data for chapter I was collected.

Neutrons have the advantage of being scattering angle independent (De Graef and McHenry 2007) and do not scatter from electron clouds due to their neutral charge. Rather they are scattered from the nucleus. The volume of a nucleus can be written as:

$$\frac{4}{3}\pi r_N^3 = \frac{4}{3}\pi r_n^3 A \qquad \text{Eq. 6}$$

where r_N is the radius of the nucleus, r_n ~ 1.5 × 10^{-15} m, and A is the atomic weight. A will always be <250 so r_N will always be <10^{-14} m or 0.001 Å. Therefore the nucleus can be treated like a point source, or δ-function, a major difference between neutron diffraction and either x-ray or electron diffraction. The intensity is uniform, not a function of scattering angle and therefore does not fall off due to form factor. The wave functions are shown as the following for neutron (Eq. 7), x-ray (Eq. 8), and electron (Eq. 9), respectively, and show the lack of angle dependence for neutrons; $\mathbf{k}'$ is the wave vector for the scattered wave, r_p is wavefront position, b is neutron scattering length, and θ the scattering angle.

$$\psi_n = \left(\frac{-b}{r_p}\right)\exp\left[-i\mathbf{k}'\cdot r_p\right] \qquad \text{Eq. 7}$$

$$\psi_x(\theta) = \left(\frac{f^x(\theta)}{r_p}\right)\left[\frac{-e^2}{4\pi m_e c^2}\right]\left[\frac{1+\cos^2(\theta)}{2}\right]\exp\left[-i\mathbf{k}'\cdot r_p\right] \qquad \text{Eq. 8}$$

$$\psi_e(\theta) = \left(\frac{f^e(\theta)}{r_p}\right)\exp\left[-i\mathbf{k}'\cdot r_p\right] \qquad \text{Eq. 9}$$

where m_e is the mass of an electron, c is the speed of light, and f is the atomic scattering factor. The fact that neutrons are angle independent allows for better

peak discrimination at higher angles and better determination of the atomic displacement parameters. This is helpful in the hydrate system where there is always movement from the occluded gas molecules.

The hydrates studied in chapter I contains D and O in the framework, and in different cases H, C, and O as the guests, which are all relatively low Z elements. X-rays interact directly with the electron cloud, and therefore the scattering potential scales with Z, the higher Z, the better the scattering (Figure A - 17). This reduces the ability of x-rays to provide detailed diffraction data for low Z materials. The neutron scattering length, b, is directly proportional to the cross section, σ, of the nucleus as shown by:

$$\sigma = 4\pi b^2 \qquad \text{Eq. 10}$$

Since it is not a function of scattering angle, this relationship suggests that $\sigma \sim 4\pi r_N^2$ (De Graef and McHenry 2007) which can be simplified to $b \approx r_N$. There are differences between elements and even between the same isotopes of elements, so b varies from element to element with positive and negative numbers based on resonance absorption in compound nucleus formation. This makes NPD an attractive technique for studying the atomic structure of materials with low Z elements such as gas hydrates.

Rietveld Refinements

Rietveld refinements of both the x-ray and neutron data were performed to ascertain atomic structural details discussed in chapters I and II. The General Structure Analysis System (GSAS) software package with EXPGUI was used for the refinements (Larson and Von Dreele 1994; Toby 2001). Rietveld refinement is an essential tool for quantitative analysis of powder diffraction data. There are a number of issues that can affect the accuracy of data collected from a powder diffraction experiment. Hugo Rietveld developed an algorithm to address these

issues resulting in a more robust analysis of the experimental data and a better determination of the refined structural details. Rietveld refinements are a least squares treatment of the observed (collected) data compared to calculated patterns where the variables of the calculated pattern are refined for a better fit to the observed data. The least squares parameters associated with the calculated pattern represent actual quantitative values for specific attributes of the material (Rietveld). The Rietveld method utilizes a pattern fitting algorithm that takes the entire pattern into consideration. Calculated intensities rather than integrated intensities are used (Rietveld 1969), and as a result it is not necessary to break the pattern into individual Bragg peaks, reducing the problems caused from the overlapping of patterns with multiphase components (Young 1995). In order to control some issues like preferred orientation, nonlinear detection systems, and primary extinction, all reflections are used. In a multiphase sample, a phase missed in the original analysis of the sample will be clearly obvious in the comparison of the calculated pattern to the observed one. Preferred orientation is probably the most serious problem to Rietveld refinement (Esteve, Ochando et al. 2000). This is significant for the research presented here since hexagonal ice (I_h), a common secondary phase found with hydrates, is well known to be prone to preferred orientation.

In order for the Rietveld method to be successful, it is desirable to have optimal sample and data collection conditions. X-ray experiments in this study were performed in Bragg Brentanno or flat plate geometry. For flat plate specimens preferred orientation is hard to avoid, and unfortunately leads to skewed relative intensities of some reflections. To model this in the x-ray powder diffraction studies the March-Dollase (March 1932; Dollase 1986) approach was used, allowing for the refinement of the preferred orientation with respect to a specific crystallographic direction (McCusker, Von Dreele et al. 1999). However, compensating for preferred orientation is not ideal, and avoidance by careful sample preparation or experimental set-up if possible is preferred. A finely

ground and well-packed sample with a smooth surface is best, however, this is extremely difficult with hydrate samples that require cold loading.

A model of the atomic structure (crystal system, lattice parameters, space group, atomic positions, atomic displacement parameters, and site occupancy factors) is needed to begin refinements, the closer the model is to the correct crystal structure the better the initial fit. The hydrate framework or host (H_2O) structure is well known and was obtained from the Inorganic Crystal Structure Database (ICSD). For the mixed gas hydrates (chapter I) the moving gas molecules were modeled individually as a sphere or concentric spheres. To create these shells of scattering density, symmetry was exploited by determining atomic positions of sites with the maximum multiplicity. Subsequently rigid bodies were created as a more sophisticated method of modeling the moving gas molecules (more details are given in chapter I). Without a fairly close structural model and good identification of the phases present the use of the Rietveld method can result in inaccurate results. Without the proper atomic positions, the Rietveld algorithm will try to correlate all the electron densities to an incorrect model, and result in a false minimum (McCusker, Von Dreele et al. 1999).

For both the x-ray and neutron data a multi-term Simpson's rule integration of the pseudo – Voigt function was used for peak fitting (Larson and Von Dreele 1994). Since the key to the Rietveld method is using the peaks separately, the peak fitting process is most important for a successful refinement. The goodness of fit for the final results is only as good as the polynomial fit to the pattern. Peak fitting is nontrivial (McCusker, Von Dreele et al. 1999).

Once the model is well defined and the peaks are fitted, this information is used with the observed diffraction pattern to refine structural parameters of the various phases present, as well as quantitative phase fractions of the sample. A least squares analysis is used to bring the calculated intensities close to the observed intensities. The M function shown below represents groups of overlapping reflections and is minimized in the process of executing a least squares refinement:

$$M = \sum_i W_i \left\{ y_i(obs) - \frac{1}{c} y_i(calc) \right\}^2$$ Eq. 11

where W_i is a halfwidth parameter, y_i is the atomic coordinate of the ith atom, and c is the overall scale factor such that $y(calc) = c \bullet y(obs)$ (Rietveld 1969).

Refining continues until the maximum shift and estimated standard deviation (esd) of the last cycle is <1, and convergence is achieved (McCusker, Von Dreele et al. 1999). Some combinations are helpful for convergence. Other parameters to include in the refinement are scale (associated with the phase fractions), site occupancy factors (sof), and atomic displacement parameters (ADPs). These parameters all contribute to the intensity of diffraction maxima, are more sensitive to background than are the positional parameters, and are highly correlated (McCusker, Von Dreele et al. 1999). However, early in the refinement, refining too many parameters at once will often cause the function to diverge.

Intensity is related to the phase abundance in a multiphase sample (Esteve, Ochando et al. 2000). Fitting the curve properly and calculating the intensity properly helps to accurately determine the amounts of phases. Due to the presence of I_h in hydrate samples, quantitative phase analysis was used on all diffraction analyses. Phase fractions amounts were used in the kinetic studies of chapter 2. Phase fractions are calculated based on the weight fraction, w_i, of the ith crystalline component from the corresponding refined scale parameter, S_i through,

$$w_i = \frac{S_i M_i V_i}{\sum_j S_j M_j V_j}$$ Eq. 12

where M_i is mass of the unit cell, and V_i is volume. $\sum_i w_i = 1$ is the normalization condition on which the algorithm is modeled (Gualtieri 2001). This normalization assumes any amorphous component as part of the background,

and therefore does not include it. It is unlikely in the studies reported here that there is a large amorphous content.

A measure of how well the refinement has worked is determined by various residuals. The weighted-profile R value, R_{wp}, is:

$$R_{wp} = \sqrt{\frac{\sum_i w_i \left[y_i(obs) - y_i(calc) \right]^2}{\sum_i w_i \left[y_i(obs) \right]^2}} \qquad \text{Eq. 13}$$

where $y_i(obs)$ is the observed intensity at step i, $y_i(calc)$ the calculated intensity, and w_i the weight (McCusker, Von Dreele et al. 1999). During the refinement process the numerator is minimized. Background treatment plays a significant role in the R_{wp} value. Comparing these values between different types of powder experiments is cautioned. If the background has been subtracted, then $y_i(obs)$ represents the net intensity. On the other hand if the background has been refined, $y_i(obs)$ will most likely include contribution from the background leading to a low R_{wp} if the background is high. Laboratory x-rays have R_{wp} values on the order of 10%, while neutron time of flight data is on the order of just a few %. The backgrounds used for the refinements reported here were fit graphically and the variables were not refined.

R_{exp} is the R value that is expected based on the counting statistics or data quality:

$$R_{\exp} = \sqrt{\frac{N - P}{\sum_i^N w_i y_i(obs)^2}} \qquad \text{Eq. 14}$$

where N is observed data points and P is the number parameters. When N is large due to high collection times, R_{exp} will be very small, which will in turn gives large χ^2 values (Eq. 15).

$$\chi^2 = \frac{R_{wp}}{R_{\exp}}$$ Eq. 15

This is known as the goodness of fit; this value should approach 1 (McCusker, Von Dreele et al. 1999). The effect of over counting can be seen in the small reported R_{exp} values for the neutron data collected on POWGEN.

R_{Bragg} (Eq. 16) reported here as R_p is a way to monitor the structural model but does not play an active role in the refinement process.

$$R_{Bragg} = \frac{\sum_{hkl} I_{hkl}(obs) - I_{hkl}(calc)}{\sum_{hkl} I_{hkl}(obs)}$$ Eq. 16

The refinement can be improved and continued until the R values are acceptable. Although the R values are good for guidance, more important are the calculated to observed fit and whether or not the chemistry and details of the structural model are logical (McCusker, Von Dreele et al. 1999).

CHAPTER I
MOLECULAR VISUALIZATION OF CH_4 – CO_2 SOLID SOLUTION IN GAS HYDRATES VIA HIGH-RESOLUTION NEUTRON POWDER DIFFRACTION

The text of this chapter was originally submitted by S. Michelle Everett, Claudia J Rawn, Bryan C. Chakoumokas, David J. Kefer, Ashfia Huq, and Tommy J Phelps to Chemistry of Materials.

This manuscript is presented as submitted. The primary author performed all of the experimental work, data analysis and original manuscript; co-authors added value by guiding experiments, examining analysis results and offering editorial suggestions for publication.

Abstract

The exchange of CO_2 for CH_4 in natural gas hydrates is an attractive approach to produce energy while simultaneously sequestering CO_2. In addition to the energy and environmental implications, the solid solution of clathrate hydrate $1\text{-}x(CH_4)x(CO_2) \bullet 5.75H_2O$ provides a model system to study how the distinct bonding and shapes of CH_4 and CO_2 influence the structure and properties of the compound. High-resolution neutron diffraction was used to examine mixed CO_2/CH_4 gas hydrates. CO_2-rich hydrates had smaller lattice parameters, which were attributed to the higher affinity of the CO_2 molecule interacting with H_2O, and resulted in a reduction in the unit cell volume. Images of experimental nuclear scattering densities illustrate how the cage occupants and energy landscape change with composition. These results provide important insights on the impact and mechanisms for exchanging CH_4 and CO_2.

Background

The search for energy sources to ease environmental and political issues of conventional sources has encouraged scientists to look to the sun, the plants, and the ocean for answers. Found at moderate pressure, low temperature conditions such as the ocean floor and subsurface permafrost regions, natural gas hydrates constitute a valuable potential source of methane (Makogon 1987; Koh and Sloan 2007). The amount of carbon stored in natural gas hydrates is

estimated to be twice that of all other carbon sources combined (Suess, Bohrmann et al. 1999). Over the past 15 years the idea of harvesting methane from natural hydrate deposits while simultaneously sequestering industrially produced CO_2 has been tantalizing (Ripmeester and Ratcliffe 1998; Brewer, Friederich et al. 1999; Lee, Seo et al. 2003; Qi, Ota et al. 2011). As envisioned, CO_2 is pumped deep into the sediment layers where natural hydrates are found. The CO_2 replaces CH_4 in the hydrate structure, and CH_4 is released. This conceptually simple process involves great engineering challenges, and a detailed understanding of the mechanisms and crystallographic response to the exchange of CO_2 molecules for CH_4 molecules is key to understanding the implications of a large-scale adoption of this strategy.

Methane hydrate most commonly adopts cubic structure type I (sI) (Schicks and Ripmeester 2004), as does CO_2. Two small cages (SC) and six large cages (LC) of hydrogen-bonded water molecules make up the sI clathrate hydrate unit cell. Figure A - 18 shows how one of each of those cages is placed crystallographically inside the unit cell. CO_2 hydrate is more thermodynamically stable at temperatures below 10 °C (Ohgaki, Takano et al. 1996; Kang, Chun et al. 1998; Anderson, Llamedo et al. 2003) than CH_4 hydrate, and the stability of CO_2 hydrate requires considerably less partial pressure at a given temperature than CH_4 (~2 MPa at 4 °C vs. ~4 MPa for methane hydrate (Adisasmito, Frank et al. 1991; Adisasmito and Sloan 1992)). Molecular dynamics simulation found the Gibbs free energy for CO_2 gas exchange in CH_4 hydrate is negative (Yezdimer, Cummings et al. 2002), indicating it is thermodynamically favorable to replace CH_4 with CO_2 in gas hydrate (Geng, Wen et al. 2009). Yuan et al. (Yuan, Sun et al. 2012) proposed that CO_2 exchange takes place by a reconstructive transformation, whereby the CH_4 hydrate first dissociates, and then the water reforms hydrate choosing from the dissolved mixture of CO_2/CH_4 gas. The placement and cage occupancy of the gas molecules during this process dictates the change in structure, which is critical for seafloor stability.

In this study, we examined the structural changes of gas exchange on sI hydrate via high-resolution neutron diffraction over a CH_4/CO_2 hydrate solid solution series. Samples were synthesized from liquid water and CO_2/CH_4 gas, closely representing the natural process where the water crystallizes around the gas molecules as they bubble up and dissolve in the seawater. Salts are excluded in the formation. Using this synthesis route, the preference of the two cage types for one gas or the other could be established in the hydrate formation process. We made pure samples of each end-member as well as 3:1, 1:1, and 1:3 CH_4/CO_2 target ratios to establish a sample series across most of the compositional range.

Experimental

Sample Synthesis. 10 mL of liquid D_2O was mixed with 1 mg of Snomax® (an ice nucleating protein made from *Pseudomonas syringae 31a*). This solution was then placed in a 450 mL Parr vessel with steel bars used for milling media. The vessel was sealed and evacuated. Each sample was pressurized with gas to 600 psi. The amount of each type of gas was sample dependent. There were 5 samples, 100% CH_4, 75% CH_4/25% CO_2, 50% CH_4/50% CO_2, 25% CH_4/75% CO_2, and 100% CO_2. In the mixed samples CO_2 was introduced first for consistency in sample prep. The pressure vessel was stored in a cold room at 2 °C on a tumbler and was tumbled constantly for 5 days at 30 RPM. The dropping pressure that is associated with hydrate formation was monitored. Hydrate formation was assumed to be complete when the pressure stopped dropping. Usually 3 to 4 days into the synthesis the vessel was brought out to room temperature for about 15 − 20 minutes, then back in the cold room on the tumbler. Before collecting the samples, they were placed in a deep freezer at -20 °C for a number of hours. If the milling media were still moving inside the vessel, the water was assumed converted into hydrate. The samples were depressurized, quenched in liquid N_2, collected, and stored in liquid N_2. The

samples were synthesized using deuterated water, and isotopically natural CH_4. This choice creates a natural contrast in the measurements; H atomic scattering density has an opposite sign from O, which creates strong contrast between CH_4 from CO_2 as guest occupants.

Neutron Data Collection. Samples were loaded into vanadium cans (OD=10 mm). Neutron powder diffraction data was collected at the Spallation Neutron Source at Oak Ridge National Lab on the POWGEN time of flight diffractometer. Data was collected using center wavelengths 1.333 Å and 2.665 Å providing a range from 0.42 − 6.18 Å in d-spacing at 10 K. In order to avoid solid N_2 at this temperature, the V cans were evacuated and backfilled with chilled He, 3 to 4 times. It was successful for 4 of the 5 samples. In the one sample where N_2 was found, it was <7% of the total sample.

POWGEN was chosen for its high-resolution capabilities along with the availability of high Q data. High Q data are imperative for resolving low d-spacing peaks, which are needed to model nearly freely rotating gas molecules with no primary chemical bonding to the crystalline lattice, and to determine details including occupant types, abundance of occupants, and atomic displacement parameters (ADPs). Figure A - 19 shows the 50% CH_4 sample after refinement. A low d-spacing section is shown to demonstrate high-resolution. Inelastic neutron scattering has previously shown that the methane molecules in methane hydrate are almost freely rotating (Tse, Ratcliffe et al. 1997; Gutt, Asmussen et al. 1999; Kamiyama, Seki et al. 2008), and neutron powder diffraction has shown that CO_2 molecules in CO_2 hydrate have a restricted but unresolved libration and large displacements (Ikeda, Yamamuro et al. 1999). This study shows real-space, static depictions of distributions of the molecular scattering densities of each cage size by way of Fourier transforms of the diffraction data, and the extended Q-range data from POWGEN ensures high fidelity. Experimental specifics can be found in Table A - 1.

Rietveld Refinement. GSAS (Larson and Von Dreele 1994) along with EXPGUI (Toby 2001) were used for Rietveld refinement of the data. In the

refinements, a rigid body treatment of the gas molecules was employed. A rigid body fixes the atoms of a molecule to be bound together at certain bond lengths and bond angles and allows the body to be treated as a discrete unit (Lake and Toby 2011). The benefit of this is to reduce the number of refineable parameters, to make the refinements less influenced by statistical uncertainty. The movement of the molecule was then handled by TLS tenors (translation, libration, and screw) instead of individual vectors for each atom of the molecule. The high symmetry of sI hydrate's space group, $Pm\bar{3}n$, further reduced the number of TLS elements. Once the rigid bodies were defined in the phase of the refinement, the occupancies of the rigid bodies were refined. At first the occupancies were constrained to hold the cages as fully occupied and in a 3:1 ratio LC:SC. That restraint was then relaxed and the residuals decreased. This indicates that the technique of neutron diffraction for structural investigation is statistically sensitive to cage occupancy, and therefore a good characterization method. Specifics on the refinements can be found in Table A - 2.

Results and Discussion

Data resulting from Fourier difference analysis were exported for use in VESTA (Momma and Izumi 2011) to provide graphical visualizations of the gas molecules inside their crystal structures. For the visualizations, the host lattice was accounted for in the refinement model while the gas molecules were removed from the model, so that the Fourier difference map revealed the nuclear scattering density distributions within the cages (Figure A - 20a,b). These maps represent a time average nuclear density of the molecules inside the clathrate structure over the collection time, which is a real space approach (Takeya, Udachin et al. 2010) to hydrate analysis through gas visualization. C and O both have positive bound coherent scattering lengths, while H is negative (6.646, 5.803, -3.739 fm, respectively). The density maps, with positive scattering density in yellow and negative in blue, clearly indicate the occupants in the LCs and the

SCs, and verify that for the pure samples only CO_2 or CH_4 exist in the cages. The nuclear density maps for the pure samples provide reference points of comparison for the three mixed-gas samples. A blending of the mixed gases and their decreasing CH_4 content is evident in the morphing of the nuclear density maps from one end-member to the other. Gas molecules are superimposed on the nuclear density maps to give a spatial sense of the map relationship to the molecules themselves. The LCs appear to confine CO_2 molecules to (010) planes of motion due to cage size and surface potential restrictions, but the more symmetrical SC allowed CO_2 molecules to move equally in all directions. Methane appears to be free to oscillate isotropically in either size cage, which is expected given its smaller molecular van der Waals radius and tetrahedral shape (Sloan and Koh 2007).

The density maps show little evidence of CH_4 in the large cage of the nominal 25% CH_4 sample. In fact, the large cages of all mixed samples show reduced CH_4, while the small cages show less CO_2. Table A - 3 contains the refinement results of the full structure including gas molecules, revealing the various site occupancies, and further supporting the visually identified gas mixtures and cage occupants. When CO_2 is present as 50% or greater of the feed gas, the structure accommodates the larger molecule in the smaller cage contrary to the speculation that CH_4 would be the only gas accepted in the small cage (Ota, Morohashi et al. 2005), showing evidence of the higher susceptibility for CO_2 hydrate formation (Adisasmito, Frank et al. 1991). Yet, overall there is a greater percentage of CH_4 in the small cages and CO_2 in the large ones. These results also confirm that not all cages are completely filled throughout the structure. Vacancies in both sized cages, and evidence of CO_2 in the smaller cage, shows potential for structural change in the hydrate reservoir during gas exchange. Additionally, these results have important implications for computational studies of gas hydrates since the amount and location of the gas molecules are important starting parameters.

CSMHYD (Sloan 1998) was used to predict CH_4/CO_2 occupancies and vacancies based on the same conditions used in this experiment. Figure A - 21 compares those results to the results from Rietveld refinement. CH_4 occupancies are very comparable between theoretical and experimental. In both cases the occupancy is less than the feed gas amount for $CH_4 \leq 75\%$. Experimental vacancies are more than predicted, but could be attributed to overcoming disorder in the system in the diffraction analysis. Overall the experimental results appear to be within reason of the theoretical results.

Figure A - 22a shows the variations of lattice parameters with the experimentally refined CH_4 composition. The lattice parameter decreases with a Vegard's Law type behavior as the CH_4 content decreases, resulting in a 0.25% reduction in unit cell volume from pure CH_4 hydrate to pure CO_2 hydrate, contrary to the expectation that the lattice parameters would increase as the amount of the larger CO_2 molecule increased, when considering the van der Waals radii of these two gases (Sloan and Koh 2007). One plausible explanation for this anomalous behavior could be attributed to greater ADPs for the smaller, lighter molecule. Due to a smaller molecular mass and tetrahedral shape, the CH_4 molecule should be able to move more freely (Kuhs 1992) and to push on the structure causing it to expand. Again an anomalous behavior was observed, and larger ADPs were refined for the pure CO_2 hydrate (Figure A - 22b). The refined ADPs for the CO_2 molecules occluded in the LCs are significantly larger than the ADPs refined for the CH_4 molecules contained in either the LC or SC. At the same time, the refined ADPs for the CO_2 molecules in the SCs are only slightly larger than those refined for the CH_4 molecules contained in either the LCs or SCs.

ADPs are highly correlated with site occupancy and absorption. One cause of disorder in this system is occupancy of the cages. The more fully occupied the hydrate is, the more disorder due to the movement of the gas. A fuller structure means more moving molecules. By comparing the ADP trend of the large and small cages and the percentage of cages full, the large and small

cages' ADPs trend down from pure CO_2 to 75% CO_2, as does the overall cage occupancy, from 100(6)%-70(3)%. Both ADPs and cage occupancies then trend back up for 100% CH_4, indicating the strong relation between ADPs and molecular movement in the structure.

The argument that there is a positive correlation between lattice parameters and ADPs is based on entropic arguments in which the energy landscape within the cage is relatively constant, allowing the occluded species to explore the entirety of the cage volume. This assumption is valid for CH_4, which is a non-polar molecule, resulting in weak energetic interactions with the framework water molecules. Consequently, the shape of the adsorption site for pure CH_4 (Figure A - 20c) is approximately spherical, mimicking the shape of the cage. The same assumption is not valid for CO_2, which has a permanent quadrupole, resulting in a non-negligible energetic interaction with the framework. Moreover, previous work has shown that a significant portion of the large displacement of the CO_2 molecule is due to its positional disorder in the large cage (Circone, Stern et al. 2003).

When energetics are important, ADPs are not only guided by molecular weight or cage size, but are dominated by adsorption site size, defined by the energy landscape within the cage. This behavior can be seen in the nuclear density data (Figure A - 20c). The CO_2 nuclear density volumes in the LCs are anisotropic and do not mimic the shape of the cage. As the isosurface level is increased to the point that only the energy maxima sites are shown, one observes that for CO_2 the ADP is averaging localization in 4 distinct sites. The anisotropy of the CO_2 molecule is evident in the multiple views, where it exhibits a disc type motion. On the other hand, the CH_4 is much more spherical and shows no preferred sites, thus explaining the larger ADP of the CO_2. The electrostatic attraction between CO_2 and H_2O may also serve to reduce the lattice constant for the CO_2 hydrate, pulling in the water matrix as it bounces between the 4 maxima. The energy landscape in the small cage is not as influential, because both CO_2 and CH_4 are isotropic in that site.

Another interesting anomaly is that the volumes of LCs and SCs did not increase uniformly with increasing lattice size. LC volume increased with increasing CH_4 content, while SC volume decreased (Figure A - 22c,d). SCs had the largest volume in the pure CO_2 sample, again pointing to the tight fit of CO_2, and LCs had the largest volume when they contained the smaller CH_4 molecule. Klapproth et al. reported an overall larger cage volume ratio V_{SC}/V_{LC} for CO_2, explained by the larger SC without much change in the LC, where we found them to be approximately the same, 0.69 for CH_4 and 0.70 for CO_2, due to the LC compensation. LCs dominate the structure by a 3:1 ratio, so their increase in volume dictates the overall increase of the lattice parameters as the CH_4 content increases.

The occupants of the cages play a role in the density of the structure (Figure A - 23). The hydrate becomes denser than seawater at ~34% when calculated based on the experimental results. Those include the formula weight determined from the refined site occupancies and unit cell volumes. Using a Vegard's law extrapolation of the lattice parameters to estimate volume of a completely filled H_2O structure, the transition occurs at a much higher percentage of CH_4, ~81%. This outcome indicates that the vacancies of the cages and the preference for CO_2 in the structure are significant structural factors when estimating the resulting physical behavior during exchange. These structural changes must be anticipated and considered when dealing with changing properties of large amounts of hydrate in the seafloor.

Conclusion

In this synthesis where hydrates were formed with liquid water and CO_2/CH_4 in gas phase, the water was free to select gas molecules from the headspace during hydrate formation, indicating a strong preference of occupants based on the phases present at the time of formation. As shown here, these occupants set the tone for the overall structure. CO_2 molecules were evident in

small cages in contradiction to most speculation, and the permanent quadrupole aspect of the CO_2 molecule had an affect on the lattice parameters. This study and future studies like it will facilitate better exchange models for predicting outcomes when recovering CH_4 from natural gas hydrates. This method of synthesis and neutron diffraction characterization provide a powerful combination to vary composition and temperature of mixed gas hydrates for solid solution determinations and structural, volumetric physical property changes, thus paving the way for successful exchange that allows utilization of natural gas hydrates for CO_2 sequestration and clean energy production.

CHAPTER II
KINETIC STUDIES OF METHANE HYDRATE DECOMPOSITION VIA LOW TEMPERATURE X-RAY POWDER DIFFRACTION

The text of this chapter was originally submitted by S. Michelle Everett, Claudia J. Rawn, Derek L. Mull, E. Andrew Payzant, and Tommy J. Phelps to Journal of Physical Chemistry A.

This work is presented as submitted. The primary author performed all of the experimental work, data analysis and original manuscript; co-authors added value by guiding experiments, examining analysis results and offering editorial suggestions for publication.

Abstract

Gas hydrates are known to have a slowed decomposition rate when held isothermally at ambient pressure and temperatures below the melting point of ice. This is termed “self-preservation” or “anomalous preservation.” As hydrate exothermically decomposes, gas is released and water of the clathrate cages transforms into ice. In the following study two regions of slowed decomposition for methane hydrate, 180 – 200 K and 230 – 260 K, were observed, and the kinetics were studied by *in situ* low temperature x-ray powder diffraction. The kinetic rate constants, k_a, reaction mechanisms, n, and activation energies, E_a, for ice formation from the decomposition of methane hydrate were determined by the Avrami model along with the Arrhenius equation. The activation energy for 180 – 200 K was 42 kJ/mol, and for 230 – 260 K was 22 kJ/mol.

Background

Gas hydrates are ice-like inclusion compounds belonging to the clathrate family, in which gas molecules are trapped inside cages formed of hydrogen-bonded water molecules (Davidson 1973; Sloan and Koh 2008). Under moderate to high pressure conditions and/or low temperatures, water molecules crystallize around gas molecules forming cages (Van der Waals and Platteeuw 1959). These guest gas molecules do not have primary bonding to the host lattice, but instead interact through van der Waals forces. The two most common

types of gas hydrate structures found in nature are structure I (sI) and structure II (sII) (Stackelberg and Muller 1954). Structure formation is based on the size of the occluded molecule (Sloan 2003). Guests ranging from 4 – 5.5 Å form sI; guests <4 Å or >6 Å form sII. Mixed gases can form either sI or sII. The water lattice is not stable without a minimum amount of gas-filled cages (Koh, Sloan et al. 2011). Methane hydrate forms sI hydrate, and if all the cages are filled with methane molecules a ratio of 46 water molecules to 8 methane molecules results. There are 2 pentagonal dodecahedral (5^{12}) cages and 6 tetrakaidecahedral ($5^{12}6^2$) cages that form the sI methane clathrate unit cell (Gupta, Dec et al. 2007).

It is well known that there are immense naturally occurring methane hydrate reservoirs in the ocean floor and permafrost regions (Suess, Bohrmann et al. 1999; Boswell 2009; Boswell and Collett 2011; Koh, Sloan et al. 2011). Estimates put the amount of carbon stored in hydrates at about twice that of all other known sources combined, including natural gas, crude oil and coal (Koh, Sloan et al. 2011). Over 230 reservoirs in 79 countries have been identified (Sun, Li et al. 2011). Hydrate reservoirs are dependent on temperature and pressure for stability, and changes in the stability field will cause the gas to be released. As climate change potential increases, reservoirs are in danger of disruption from an overall temperature increase (Kroeger, di Primio et al. 2011). Models predict the Arctic Ocean will be most affected by a temperature increase. In fact, the Arctic permafrost regions have already begun to decompose (Kvenvolden 1988; Kvenvolden 1988). The immediate concern arises from the accidental discharge of methane due to oil/gas drilling for new deposits. Deposits in Russia contain self-preserved hydrates (Yakushev and Istomin 1992), thus drilling would disrupt the pressure and easily prompt these highly unstable formations into immediate decomposition.

Methane hydrate has a well-defined stability zone of temperature and pressure, within which it is stable (Sloan and Koh 2008). When removed from the thermodynamically stable zone, hydrates decompose, releasing methane. In

the case of ambient pressure, below 273 K, thermodynamically stable hexagonal ice I_h and gas result from hydrate decomposition (Stern, Circone et al. 2001; Takeya, Shimada et al. 2001; Circone, Stern et al. 2003; Kuhs, Genov et al. 2004; Takeya, Uchida et al. 2005; Ogienko, Kurnosov et al. 2006). There is some recent evidence that under certain conditions, in some gas hydrates, supercooled liquid water is present after dissociation (Takeya, Nango et al. 2005; Melnikov, Nesterov et al. 2009; Melnikov, Nesterov et al. 2012). Under temperature and pressure conditions outside of the stability zone, a number of gas hydrates (N_2, Ar, Kr, CF_4, CO, CO_2, and CH_4) (Takeya and Ripmeester 2008) exhibit periods of slowed decomposition when held isothermally, referred to synonymously as either “self-preservation” or “anomalous preservation.”

Anomalous preservation of methane hydrates has been well documented in both synthetic and recovered naturally occurring samples (Davidson, Garg et al. 1986; Handa and Stupin 1992; Dallimore and Collett 1995). In the early 2000s, a number of publications provided an understanding of the anomalous preservation phenomena (Kuhs, Klapproth et al. 2000; Stern, Circone et al. 2001; Takeya, Shimada et al. 2001; Takeya, Ebinuma et al. 2002; Stern, Circone et al. 2003; Kuhs, Genov et al. 2004; Takeya, Uchida et al. 2005). A generally accepted temperature-dependent decomposition model was proposed by Stern et al. (Stern, Circone et al. 2001) that highlighted an increasing, monotonic decomposition regime from 193 K, with significantly decreased decomposition kinetics beginning around 240 K and ceasing just under 273 K. Decomposition rates were observed to exhibit two minima at 250 and 268 K. Given enough time in this temperature range hydrate will fully dissociate. Takeya et al. (Takeya, Uchida et al. 2005) reported results acquired using a combination of confocal scanning microscopy and energy dispersive x-ray diffraction; they stated that the particle size of the ice is a determining factor for anomalous preservation. Kuhs et al. (Kuhs, Genov et al. 2004) used *in situ* neutron diffraction studies and based on their results suggested that defects were annealed at ~240 K, causing the onset of anomalous preservation.

Kinetic studies of methane hydrate decomposition are typically either treated as an intrinsic kinetic process or a moving boundary heat transfer problem (Clarke and Bishnoi 2001). Ullerich et al. (Ullerich, Selim et al. 1987) suggested that water was carried away from the bulk hydrate as methane was released, suggesting moving boundary heat transfer, whereas Kim et al. (Kim, Bishnoi et al. 1987) presented an intrinsic kinetics approach. By combining these methods, Jamaluddin et al. (Jamaluddin, Kalogerakis et al. 1989) showed that pressure determines whether the process is strictly based on heat transfer or both heat transfer and intrinsic kinetics.

Kim et al. (Kim, Bishnoi et al. 1987) investigated the activation energy of methane hydrate decomposition by using a semi-batch reactor where methane was vented from the system. The pressure was held just below the triple point phase equilibrium pressure for the corresponding temperature, giving a pressure range of 0.17 – 6.97 MPa for temperatures of 274 – 283 K. Hydrate dissociation was estimated by recording moles of released methane, resulting in E_a = 78.3 kJ/mol. Clarke et al. (Clarke and Bishnoi 2001) developed a model, which built on the work of Kim et al. including the added information of particle size, relating it to the diffusion of methane away from the bulk. This system also measured moles of released methane, however in a closed system. The conditions were: 3.1 – 6.1 MPa and 274.65 – 281.15 K, resulting in E_a = 81 kJ/mol. Takeya et al. (Takeya, Shimada et al. 2001) determined diffusion coefficients based on a scaled radius model using integrated intensities from energy-dispersive x-ray data. At ambient pressure and a temperature range of 168 – 198 K an E_a = 20.1 kJ/mol was calculated.

The objective of this study was to investigate the differences of the kinetics in two different temperature ranges exhibiting anomalous preservation in methane hydrate. This was accomplished by isothermally decomposing synthesized methane hydrate, while collecting *in situ* low temperature x-ray diffraction data for analysis using Avrami's nucleation and crystal growth model (Putnis 1992). By collecting temperature dependent x-ray diffraction data on

methane hydrate three regions of slowed decomposition were observed. The rate constant, k_a, mechanism-dependent kinetic constant, or the Avrami exponent, n, and the activation energies (E_a) of two of those regions based on Avrami models and Arrhenius plots (Kim, Kim et al. 2005; Ayturk, Payzant et al. 2008; Kim, Payzant et al. 2008) were determined using isothermal x-ray diffraction data. The assumption made in the Avrami model is that the new phase is independent from the original phase growing randomly and uniformly, until one single crystal collides with growth from another (Ayturk, Payzant et al. 2008). Phase transition from cubic sI hydrate to ice can be thought of as a solid-solid phase transition, even though gas is liberated. Throughout most heterogeneous mineral reactions the original phase is separated from the new phase by some sort of interface caused by the nucleation and growth of the new phase (Putnis 1992). Here the nucleation of ice from methane hydrate dissociation was studied. There were two processes occurring during the solid-solid phase transition, atoms from the original phase were diffusing to the new growth, and then they were combined with the newly established surface structure. The experimentally observed E_a was a function of both the diffusive and combinatory processes (Putnis 1992).

Experimental

Hydrate Sample Preparation. H_2O was frozen in thin layers, crushed with a mortar and pestle in liquid nitrogen, and sieved to a 500 μm or less particle size. The crushed ice was placed in a 450 mL Parr vessel chilled to 77 K. The pressure vessel was packed in ice and the atmosphere was evacuated. The vessel was subsequently pressurized with cold CH_4 to 300 psi and placed in a freezer at 253 K. The pressure was recorded daily for 10 days, and the vessel was shaken to promote even diffusion of the gas into the ice. The formation of hydrate was deemed complete when the pressure ceased to drop. The vessel was rapidly depressurized, and immediately quenched in liquid N_2 to preserve

the hydrate. Three nominally similar samples were synthesized, and subdivided for data collection. They will be referred to as S1, S2, and S3.

Low Temperature X-ray Diffraction (LTXRD). Liquid N_2 quenched samples were cold loaded onto an Anton-Paar TTK450 low temperature reaction chamber. LTXRD data were collected using a PANalytical X'Pert Pro MPD diffractometer, equipped with an X'celerator detector that enabled fast data collection using Cu K_α radiation at 45 kV and 40 mA. Data were collected between 10° − 70° (2θ) so that each scan took approximately 10 minutes. First, a subsample of each of the three samples was decomposed using an isochronal annealing procedure over the temperature range of 140 − 260 K. Second, subsamples of each of the three samples were decomposed isothermally over time at specific temperatures within two temperature ranges, 180 – 200 K and 230 – 260 K. Phase fractions of hydrate and ice I_h were refined by Rietveld analysis from the data using the General Structural Analysis System (GSAS) (Larson and Von Dreele 1994) and EXPGUI (Toby 2001).

Results and Discussion

LTXRD data were collected on the three nominally similar samples. Each sample was first decomposed as a function of temperature while x-ray diffraction data were collected. As can be seen in Figure A - 24, all three samples exhibited a similar overall decomposition scheme even though the initial ratio of hydrate to ice varied. There are three regions of slowed decomposition and two regions of more rapid decomposition. Region 1 of slowed decomposition was estimated to be from 140 − 160 K, region 2 was from 180 − 200 K, and region 3 was from 230 − 260 K. Once these three regions were identified, *in situ* data were collected while the samples decomposed isothermally as a function of time at various temperatures within each region of slowed decomposition. The decomposition of S1 at 250 K (Figure A - 25) was chosen to demonstrate the phase change from

hydrate to ice I_h. The phase fractions of both the methane hydrate and ice were refined from the LTXRD data.

The Avrami model is commonly used to determine kinetic information such as activation energy and heterogeneous types of crystal growth. Avrami behavior can be described by this modified equation:

$$\alpha = 1 - e^{-(k_a t)^n} \qquad \text{Eq. 17}$$

or

$$\ln[-\ln(1-\alpha)] = n \ln k_a + n \ln t \qquad \text{Eq. 18}$$

where α is the fraction transformed (in this case the percent ice formed), k_a is the rate constant, and n is the reaction mechanism (Ayturk, Payzant et al. 2008). The value of n can suggest dimensionality of crystal growth of the new phase, such as polyhedral, plate-like, or lineal (Avrami 1939). The rate constant, k_a, is dependent on the growth and nucleation and in turn is very susceptible to temperature. By plotting the ln[−ln(1 − α)] vs. ln t the slope is n and the y intercept is n ln k_a. By plotting ln k_a versus 1/T, the result is an Arrhenius plot where the slope of the linear trend is E_a/R, from which the activation energy can be determined.

Weight fractions of the increasing ice phase (α) in each isothermal decomposition scan were plotted vs. time in regions 2 (180 − 200 K) (Figure A - 26a) and 3 (230 − 260 K) (Figure A - 27b). The resulting shapes in both regions gave rise to an Avrami model analysis. The colder region, 180 – 200 K, exhibits more of a traditional Avrami type S-curve as opposed to the flatter curve seen in the warmer region, 230 – 260 K. This suggests the crystal growth is transitioning from plate-like (2D) in region 2 to lineal (1D) in region 3 (Avrami 1940). Avrami plots were constructed for regions 2 (180 − 200 K) (Figure A - 26b) and 3 (230 − 260 K) (Figure A - 27a). The coldest region (140 – 160 K) was difficult to assess due to the long reaction times, requiring extended data collection times, during

which additional ice (frost from the moisture in the atmosphere) formed on the sample, complicating the analysis. In Figure A - 26b, an Avrami plot was constructed from data collected on S3 at three temperatures in region 2 (180 – 200 K). The three linear relationships exhibited similar slopes, resulting in Avrami exponents in the narrow range of $1.33 \leq n \leq 1.36$ (Table A - 4). The fact that all three scans provided similar Avrami exponents despite the fact that they were taken at different temperatures (190, 195, and 200 K) supports the premise that within a given region isokinetic behavior occurred.

In Figure A - 27, an Avrami plot was constructed from data collected on all three samples at various temperatures in region 3 (230 – 260 K). The six linear relationships revealed similar slopes, resulting in Avrami exponents in the range of $0.59 \leq n \leq 0.75$ (Table A - 4). In order to establish that similar behavior in the hydrate decomposition was observed for different samples, prepared at different times and with different starting amounts of hydrate, all three samples were examined at 240 K. These three experiments showed quantitatively similar behavior, emphasizing the reproducibility of results. Again, the small range of Avrami exponents in this region, despite the fact that they are taken at different temperatures (from 230 − 260 K), supported the premise of isokinetic behavior within a given temperature region. The difference of $0.59 \leq n \leq 0.75$ in region 3 and $1.33 \leq n \leq 1.36$ in region 2 further supports a transition from plate-like growth in the colder region to lineal crystal growth in the warmer region. The difference also indicates anisokinetic behavior between the two regions.

In Figure A - 28 an Arrhenius plot is shown for region 2 (180 – 200 K). Each point on the plot corresponds to one set of data from the Avrami plot in Figure A - 26b where the y intercept was used to determine the value of k_a (Table A - 4). The activation energy obtained in region 2 was 42 kJ/mol. In Figure A - 29 an Arrhenius plot is shown for Region 3 (230 – 260 K). Each point on the plot corresponds to one set of data from the Avrami plot in Figure A - 27b where the y intercept was used to determine the value of k_a (Table A - 4). The activation energy obtained in region 3 was 22 kJ/mol.

Results herein differ from other E_a numbers reported by, Kim et al. (Kim, Bishnoi et al. 1987) (78.3 kJ/mol) and Clarke et al. (Clarke and Bishnoi 2001) (81 kJ/mol), likely due to differences in experimental conditions. Decomposition rates are known to be heavily affected by temperature-pressure-time conditions (Jamaluddin, Kalogerakis et al. 1989; Stern, Circone et al. 2001). The previous studies initiated hydrate decomposition via pressure change, as opposed to temperature change used in the current study. Activation energy is not a thermodynamic state variable so it is path dependent. It is reasonable that different paths to dissociation yield different values of E_a, and direct comparison is not instructive.

In this study, as the temperature increased, the activation energy decreased, potentially because the microstructure of the ice in the higher temperature range is more conducive to the rapid dissipation of heat and occluded gas than that of the colder temperature range. It has been well documented that cubic ice I_c, is formed upon heating from high-pressure ices that have been quenched and recovered at ambient pressure (Lisgarten and Blackman 1956; Shallcross and Carpenter 1957; Dowell and Rinfret 1960; Shimaoka 1960; Beaumont, Chihara et al. 1961; Sugisaki, Suga et al. 1968). The temperature range for ice I_c formation has been reported anywhere from 140 to 160 K (Beaumont, Chihara et al. 1961; Sugisaki, Suga et al. 1968), suggesting the possibility of ice I_c in region 2 (180 – 200 K). The transformation temperature from ice I_c to I_h has been reported in the range of 190 – 200 K (Beaumont, Chihara et al. 1961; Sugisaki, Suga et al. 1968), at which point the transforming ice would contain many defects from the structural transition. Takeya et al. (Takeya, Ebinuma et al. 2002) stated that the diffusion of methane from the core through the ice was grain boundary controlled and as a result larger grains would result in slower diffusion from the hydrate core and defects would result in faster diffusion. Sugisaki et al. (Sugisaki, Suga et al. 1968) also reported an increase in exothermic activity during the I_c to I_h phase change between 190 and 210 K, explaining the rapid increase in hydrate dissociation between region 2 and region

3; the amount of defects were increased and therefore the gas could more easily escape (Kuhs, Genov et al. 2004). According to Kuhs et al. (Kuhs, Genov et al. 2004) ice I_h has transformed and annealed by ~240 K, which is the onset of anomalous preservation. Similarly, we saw anomalous preservation begin in region 3 at 230 K. The higher E_a determined for the 180 – 200 K temperature range (colder region 2) compared to the E_a determined for 230 – 260 K (warmer region 3), could be explained by the different microstructures found in the different temperature ranges. Our activation energies support the premise that the diffusion path of the methane out from the hydrate core in the warmer temperature range is easier due to the microstructure of ice than that at the colder temperature range, explaining the lower activation energy found in the warmer region 3.

Studying gas hydrates with laboratory x-ray powder diffraction is difficult. It is a material composed of low z elements. Samples must be loaded cold, making it difficult to achieve flat surfaces. The secondary ice phase(s) are notorious for preferred orientation, peak broadening due to defects, and phase transformations with superimposed peak positions. For these reasons it is not surprising that Ice I_c could not clearly be identified in the diffraction data (Arnold 1968; Kuhs, Genov et al. 2004).

Others have opted to explain the variation in activation energy in terms of heat transfer rather than mass transfer; the two phenomena are coupled if the heat loss is primarily due to diffusion of released methane. Jamaluddin et al. (Jamaluddin, Kalogerakis et al. 1989) proposed that decomposition rate was due to heat transfer or a combination of heat transfer and intrinsic kinetics, and could be determined by the E_a. E_a < 63 kJ/mol corresponded to a high rate controlled by heat transfer, while E_a > 63 kJ/mol suggested the rate depended on both. Here both activation energies were ≤ 42 kJ/mol, indicating the intrinsic rate of decomposition was not a limiting step for either temperature range, and that heat transfer alone appeared to be controlling the decomposition rate. The E_a of previous studies (Kim, Bishnoi et al. 1987; Clarke and Bishnoi 2001) indicated

control by both heat transfer and intrinsic kinetics. The discrepancy between the E_a reported by Takeya et al. (20.1 kJ/mol, 168 – 198 K) and this work (42 kJ/mol, 180 – 200 K) is unclear. Both studies held samples at ambient pressure. The only obvious difference in experimental set up appears to be that a constant stream of temperature controlled N_2 was passed over the sample. It is possible this contributed to the lower E_a values of Takeya et al. by promoting the transport of CH_4 away from the sample. Another source that could have contributed to the different results is that the calculated numbers used for the Arrhenius plot in Takeya et al. (Takeya, Shimada et al. 2001) covered both fast and slow decomposition rates, where this study excluded the fast regions.

Our samples appeared to remain preserved above 230 K. Most of the temperatures in previous studies were well above 200 K, so little comparison into decomposition behavior between region 1 (140 − 160 K) or region 2 (180 – 200 K) can be remarked upon (Stern, Circone et al. 2001; Stern, Circone et al. 2003; Kuhs, Genov et al. 2004). Kinetic studies of the temperature range 140 – 160 K (region 1) will require more control over the atmosphere, particularly the humidity.

Conclusion

Methane hydrate decomposition was studied via *in situ* LTXRD, from which two temperature ranges of anomalous preservation were identified. Two of the ranges found to exhibit anomalous preservation were compared, 180 – 200 K and 230 – 260 K. The Avrami models showed the regions were isokinetic within their own temperature range and anisokinetic between the two ranges. The colder region (180 – 200 K) had an Avrami constant of n ~ 1.3, while the warmer region (230 – 260 K) had a constant of n ~ 0.7. The activation energy of the 180 – 200 K range was 42 kJ/mol, and the activation energy was 22 kJ/mol for the 230 – 260 K range. The differences between the activation energies determined here and in previous studies can be attributed to differing experimental temperature/pressure regimes. The higher E_a in the colder temperature region

(180 – 200 K) was attributed to the microstructure of ice I_c, which differs from ice I_h found in the warmer range (230 – 260 K).

CONCLUSION

Results

Gas hydrates were studied via low temperature x-ray powder diffraction and high resolution neutron powder diffraction. In the process of other hydrate studies, a new sample synthesis that took careful experimentation to develop starting with water was established, and found to be very effective in eliminating a large percentage of ice phase in the hydrate samples. Samples synthesized from ice had 40 – 60% ice, where samples made from liquid had <10 % ice.

High-resolution neutron diffraction was used to investigate mixed CO_2/CH_4 hydrates. Fourier difference maps were used to render 3D models of gas molecules in order to visualize them in large and small cages. The use of CH_4 instead of CD_4 was instructive due to the negative scattering of H_2 compared to the positive scattering of the D_2. O_2 also has positive scattering and the difference aided in the visual representations where positive and negative scattering were different colors, therefore CH4 and CO2 could be differentiated.

Rigid bodies of the gas molecules, both CH_4 and CO_2, were developed from crystallographic models, and TLS methods were used to determine the gas occupancy, CH_4 vs. CO_2, and cage preference, large vs. small. As seen in literature, CO_2 was preferred overall, as each mixed sample had a higher CO_2 ratio in the sample than in the feed gas, but CH_4 was preferential to small cages. Contrary to common findings in literature, CO_2 was seen to populate the small cages.

Lattice parameters, cage volumes, and ADPs were determined through Rietveld analysis and were compared as a function of CH_4 content. Lattice parameters increased as CH_4 content increased, despite the fact that CO_2 has a larger Van der Waals radius than CH_4. Atomic displacement parameters of CO_2 were larger than those of CH_4, explained by investigating energy maxima via nuclear scattering densities. The permanent quadrupole of the CO_2 molecule

caused it to be pulled in four distinct directions giving it larger ADPs, while simultaneously attracting the water lattice inward explaining the smaller lattice parameters.

Cage Volumes were determined from refined oxygen positions of the host lattice. Large cage volumes increased with increasing CH_4 content while small cages decreased with increasing CH_4 content. The overall lattice increase was attributed to the fact that the large cages dominate the structure 3:1, therefore netting an overall lattice increase.

Finally, the refined cage occupancies and occupants were used to compare how structure − filling affects overall density. Hydrate filled with all CO_2 is denser than water, where hydrate filled with all CH_4 is less. The experimental data showed that mixed CO_2/CH_4 hydrate would be more dense up to ~34% full, where the calculated data showed ~81%.

In the second study, low temperature x-ray powder diffraction was used to study the kinetics of CH_4 hydrate decomposition. Kinetics of solid-solid phase transition from hydrate phase to ice phase were studied through the Avrami model determining the dimensionality of crystal growth. Three regions of slowed decomposition over the range of 140 – 260 K were observed from temperature dependent x-ray data collection. Two of those three ranges were studied by collecting isothermal x-rays scans at various temperatures within the regions. The regions were found to have isokinetic behavior within their own temperature regions, and anisokinetic behavior between the two regions. In the colder region, 180 – 200 K, n ~ 1.3, and the warmer region, 230 – 260 K, n ~ 0.7.

The Arrehnius model was then used to determine activation energy. Each set of isothermal scans resulted in a kinetic constant, k_a, which was used in the Arrehnius model. The colder region had an E_a = 42 kJ/mol and the warmer had an E_a = 22 kJ/mol. The difference in the activation energies was explained by different microstructures between the regions. Gas diffuses through grain boundaries in gas hydrates during decomposition. The presence of cubic ice in the colder region was used to explain the slower diffusion. The fact that both

regions had an activation energy less than 63 kJ/mol indicates the kinetics are heat transferred controlled as well as mass controlled.

It was observed in the third region that lengthy reaction time at low temperatures allowed frost to grow on the sample in the unsealed sample chamber. The effect of sample surface displacement and sample preparation was evident as some samples had to be decomposed multiple times for the data to support quality refinement. Preferred orientation was observed as ice percentages grew over the decomposition times, which were accounted for in the refinements.

Applications and Future Studies

The mixed hydrate studies help to better understand how the exchange of CO_2 for CH_4 will occur on the atomic level. While CO_2 is being pumped into the sediment, the hydrate will begin decompose because the stability zone will be disrupted. As the hydrate reforms with CO_2, there will be varying amounts of CO_2/CH_4 solid solution. The change in lattice parameters will have an effect on the stability of the hydrate reservoir as a whole. The studies shown here indicate the volume would reduce at these temperatures. Further studies at temperatures closer to permafrost conditions would prove useful. These studies were performed at 10 K in an attempt to slow the moving gas in order to determine if this method would result in useful data. It did indeed, and now a number of gas hydrates could be studied at various temperatures in order to determine the effect of temperature and gas mixtures on cage occupancies. Currently our group is synthesizing samples for a temperature dependent study set to begin in mid-March.

In addition, an *in situ* pressure cell would give even closer results to the actual exchange process. CH_4 hydrates packed in pressure cells, at pressures representative of reservoir pressures could be studied with high resolution neutron diffraction while CO_2 was flowed. The information gained here could be

used in modeling attempts to predict large scale ground stability. The change in hydrate stability could affect its long term durability. Seafloor stability is a concern that should be considered before CH_4 extraction.

Information gained from the decomposition studies helped to further understand anomalous preservation and hydrate dissociation. A fundamental understanding of hydrate decomposition can be applied to better understand how hydrates will react to a warming global climate. Basic scientific understanding of the kinetic process could lead to better models. Quasi-elastic neutron scattering, QENS, would be a good next step to help further determine the kinetics of hydrate decomposition. This is a technique that probes samples with an energy resolution on in the μeV range. It allows for the study of diffusive and relaxational atomic and molecular motion by probing dynamic processes in the nano-second range. Rotational diffusion and translational diffusion can be determined. This experimental technique works well with molecular dynamics simulations to determine what types of motion occur in a diffusion process. Kinetic constants can also be ascertained from QENS.

A meaningful contribution was made through this study to the understanding of gas hydrates. Future work should be continued to enhance it further.

LIST OF REFERENCES

Adisasmito, S., R. J. Frank, et al. (1991). "Hydrates of Carbon Dioxide and Methane Mixtures." Journal of Chemical and Engineering Data **36**(1): 68-71.
Adisasmito, S. and E. D. Sloan (1992). "Hydrates of Hydrocarbon Gases Containing Carbon Dioxide." Journal of Chemical and Engineering Data **37**(3): 343-349.
Anderson, R., M. Llamedo, et al. (2003). "Experimental measurement of methane and carbon dioxide clathrate hydrate equilibria in mesoporous silica." Journal of Physical Chemistry B **107**(15): 3507-3514.
Archer, D., B. Buffett, et al. (2009). "Ocean methane hydrates as a slow tipping point in the global carbon cycle." Proceedings of the National Academy of Sciences of the United States of America **106**(49): 20596-20601.
Arnold, G. P. (1968). "Neutron-Diffraction Study of Ice Polymorphs. III. Ice Ic." The Journal of Chemical Physics **49**(10): 4365.
Avrami, M. (1939). "Kinetics of phase change I - General theory." Journal of Chemical Physics **7**(12): 1103-1112.
Avrami, M. (1940). "Kinetics of Phase Change II - Transformation-Time Relations for Random Distribution of Nuclei." Journal of Chemical Physics **8**: 212-224.
Ayturk, M. E., E. A. Payzant, et al. (2008). "Isothermal nucleation and growth kinetics of Pd/Ag alloy phase via in situ time-resolved high-temperature X-ray diffraction (HTXRD) analysis." Journal of Membrane Science **316**(1-2): 97-111.
Beaumont, R. H., H. Chihara, et al. (1961). "Transitions between Different Forms of Ice." The Journal of Chemical Physics **34**(4): 1456.
Boetius, A. and E. Suess (2004). "Hydrate Ridge: a natural laboratory for the study of microbial life fueled by methane from near-surface gas hydrates." Chemical Geology **205**(3-4): 291-310.
Bohannon, J. (2008). "Energy - Weighing the climate risks of an untapped fossil fuel." Science **319**(5871): 1753-1753.
Boswell, R. (2009). "Is Gas Hydrate Energy Within Reach?" Science **325**(5943): 957-958.
Boswell, R. and T. S. Collett (2006) Fire in the Ice: Methane HydrateNewsletter, 5.
Boswell, R. and T. S. Collett (2011). "Current perspectives on gas hydrate resources." Energy & Environmental Science **4**(4): 1206-1215.
Brewer, P. G., C. Friederich, et al. (1999). "Direct experiments on the ocean disposal of fossil fuel CO2." Science **284**(5416): 943-945.
Callister, W. D. (2007). Materials Science And Engineering: An Introduction, John Wiley & Sons.
Circone, S., L. A. Stern, et al. (2003). "CO(2) hydrate: Synthesis, composition, structure, dissociation behavior, and a comparison to structure I CH(4) hydrate." Journal of Physical Chemistry B **107**(23): 5529-5539.

Clarke, M. and P. R. Bishnoi (2001). "Determination of the activation energy and intrinsic rate constant of methane gas hydrate decomposition." Canadian Journal of Chemical Engineering **79**(1): 143-147.
Collett, T. S. and V. A. Kuuskraa (1998). "Hydrates contain vast store of world gas resources." Oil & Gas Journal **96**(19): 90-95.
Cullity, B. D. and S. R. Stock (2001). Elements of x-ray diffraction, Prentice Hall.
Dallimore, S. R. and T. S. Collett (1995). "Intrapermafrost Gas Hydrates from a Deep Core-Hole in the Mackenzie Delta, Northwest-Territories, Canada." Geology **23**(6): 527-530.
Davidson, D. W. (1973). Clathrate Hydrates. Water: A comprehensive treatise. F. Franks. New York, Plenum. **2:** 115 - 234.
Davidson, D. W., S. K. Garg, et al. (1986). "Laboratory analysis of a naturally occurring gas hydrate from sediment of the Gulf of Mexico." Geochimica Et Cosmochimica Acta **50**(4): 619-623.
Davy, B., I. Pecher, et al. (2010). "Gas escape features off New Zealand: Evidence of massive release of methane from hydrates." Geophysical Research Letters **37**.
Davy, H. (1811). "On some of the combinations of oxymuriatic gas and oxygene, and on the chemical relations of these principles to inflammable bodies." Philos. Trans. R. Soc. **101**: 1-35.
De Graef, M. and M. E. McHenry (2007). Structure of Materials: An introduction to crystallography, diffraction and symmetry. Cambridge, Cambridge University Press.
Demirbas, A. (2010). "Methane hydrates as potential energy resource: Part 1-Importance, resource and recovery facilities." Energy Conversion and Management **51**(7): 1547-1561.
Dickens, G. R., J. R. Oneil, et al. (1995). "DISSOCIATION OF OCEANIC METHANE HYDRATE AS A CAUSE OF THE CARBON-ISOTOPE EXCURSION AT THE END OF THE PALEOCENE." Paleoceanography **10**(6): 965-971.
Dollase, W. A. (1986). "Correction of Intensities for Preferred Orientation in Powder Diffractometry - Application of the March Model." Journal of Applied Crystallography **19**: 267-272.
Dowell, L. G. and A. P. Rinfret (1960). "Low-Temperature Forms of Ice as Studied by X-Ray Diffraction." Nature **188**(4757): 1144-1148.
Dyadin, Y. A., E. G. Larionov, et al. (1999). "Clathrate hydrates of hydrogen and neon." Mendeleev Communications(5): 209-210.
Esteve, V., L. E. Ochando, et al. (2000). "Quantitative phase analysis of mixtures of three components using Rietveld and Rius standardless methods. Comparative results." Crystal Research and Technology **35**(10): 1183-1192.
Gayet, P., C. Dicharry, et al. (2005). "Experimental determination of methane hydrate dissociation curve up to 55 MPa by using a small amount of

surfactant as hydrate promoter." Chemical Engineering Science **60**(21): 5751-5758.
Geng, C. Y., H. Wen, et al. (2009). "Molecular Simulation of the Potential of Methane Reoccupation during the Replacement of Methane Hydrate by CO(2)." Journal of Physical Chemistry A **113**(18): 5463-5469.
Genov, G. (2005). Physical processes of CO2 hydrate formation and decomposition at conditions relevant to Mars. Doctor of Philosophy, Georg-August-Universitat zu Gottingen.
Gualtieri, A. F. (2001). "A guided training exercise of quantitative phase analysis using EXPGUI." Retrieved January 24, 2013, from http://www.ccp14.ac.uk/solution/gsas/files/expgui_quant_gualtieri.pdf.
Gupta, A., S. F. Dec, et al. (2007). "NMR investigation of methane hydrate dissociation." Journal of Physical Chemistry C **111**(5): 2341-2346.
Gutt, C., B. Asmussen, et al. (1999). "Quantum rotations in natural methane-clathrates from the Pacific seafloor." Europhysics Letters **48**(3): 269-275.
Handa, Y. P. and D. Stupin (1992). "Thermodynamic Properties and Dissociation Characteristics of Methane and Propane Hydrates in 70-A-Radius Silica Gel Pores." Journal of Physical Chemistry **96**(21): 8599-8603.
Hatzikiriakos, S. G. and P. Englezos (1993). "The relationship between global warming and methane gas hydrates in the earth." Chemical Engineering Science **48**(23): 3963-3969.
Hester, K. C. and E. D. Sloan (2005). "sII structural transitions from binary mixtures of simple sI formers." International Journal of Thermophysics **26**(1): 95-106.
Ikeda, T., O. Yamamuro, et al. (1999). "Neutron diffraction study of carbon dioxide clathrate hydrate." Journal of Physics and Chemistry of Solids **60**(8-9): 1527-1529.
Jamaluddin, A. K. M., N. Kalogerakis, et al. (1989). "Modelling of Decomposition of a Synthetic Core of Methane Gas Hydrate by Coupling Intrinsic Kinetics with Heat Transfer Rates." Canadian Journal of Chemical Engineering **67**(6): 948-954.
Ji, C., G. Ahmadi, et al. (2001). "Natural gas production from hydrate decomposition by depressurization." Chemical Engineering Science **56**(20): 5801-5814.
Kamiyama, T., N. Seki, et al. (2008). Inelastic Neutron Scattering Study of Host and Guest Molecular Motions in Methane Hydrate. Proceedings of the 6th International Conference on Gas Hydrates (ICGH 2008), Vancouver, British Columbia, Canada.
Kang, S. P., M. K. Chun, et al. (1998). "Phase equilibria of methane and carbon dioxide hydrates in the aqueous MgCl2 solutions." Fluid Phase Equilibria **147**(1-2): 229-238.
Kennett, J. P. and L. D. Stott (1991). "Abrupt deep-sea warming, palaeoceanographic changes and benthic extinctions at the end of the Palaeocene." Nature **353**(6341): 225-229.

Kerr, R. A. (2004). "Energy - Gas hydrate resource: Smaller but sooner." Science **303**(5660): 946-947.
Kim, H. C., P. R. Bishnoi, et al. (1987). "Kinetics of Methane Hydrate Decomposition." Chemical Engineering Science **42**(7): 1645-1653.
Kim, W. K., S. Kim, et al. (2005). "Reaction kinetics of alpha-CuInSe2 formation from an In2Se3/CuSe bilayer precursor film." Journal of Physics and Chemistry of Solids **66**(11): 1915-1919.
Kim, W. K., E. A. Payzant, et al. (2008). "Reaction kinetics of CuGaSe2 formation from a GaSe/CuSe bilayer precursor film." Journal of Crystal Growth **310**(12): 2987-2994.
Klauda, J. B. and S. I. Sandler (2005). "Global distribution of methane hydrate in ocean sediment." Energy & Fuels **19**(2): 459-470.
Koh, C. A. and E. D. Sloan (2007). "Natural gas hydrates: Recent advances and challenges in energy and environmental applications." Aiche Journal **53**(7): 1636-1643.
Koh, C. A., E. D. Sloan, et al. (2011). Fundamentals and Applications of Gas Hydrates. Annual Review of Chemical and Biomolecular Engineering, Vol 2. J. M. Prausnitz. **2:** 237-257.
Koh, C. A., A. Sum, et al. (2010). Natural Gas Hydrates in Flow Assurance, Elsevier Science.
Kroeger, K. F., R. di Primio, et al. (2011). "Atmospheric methane from organic carbon mobilization in sedimentary basins - The sleeping giant?" Earth-Science Reviews **107**(3-4): 423-442.
Kuhs, W. F. (1992). "Generalized Atomic Displacements in Crystallographic Structure-Analysis." Acta Crystallographica Section A **48**: 80-98.
Kuhs, W. F., G. Genov, et al. (2004). "Ice perfection and onset of anomalous preservation of gas hydrates." Physical Chemistry Chemical Physics **6**(21): 4917-4920.
Kuhs, W. F. and T. C. Hansen (2006). Time-resolved neutron diffraction studies with emphasis on water ices and gas hydrates. Neutron Scattering in Earth Sciences. H. R. Wenk. **63:** 171-204.
Kuhs, W. F., A. Klapproth, et al. (2000). "The formation of meso- and macroporous gas hydrates." Geophysical Research Letters **27**(18): 2929-2932.
Kvamme, B., A. Graue, et al. (2007). "Storage of CO2 in natural gas hydrate reservoirs and the effect of hydrate as an extra sealing in cold aquifers." International Journal of Greenhouse Gas Control **1**(2): 236-246.
Kvenvolden, K. A. (1988). "Methane hydrate — A major reservoir of carbon in the shallow geosphere?" Chemical Geology **71**(1-3): 41-51.
Kvenvolden, K. A. (1988). "Methane hydrates and global climate." Global Biogeochemical Cycles **2**: 221-229.
Kvenvolden, K. A. and J. W. Harbaugh (1983). "Reassessment of the Rates at which Oil from Natural Sources Enters the marine environment." Marine Environmental Research **10**(4): 223-243.

Kvenvolden, K. A., T. D. Lorenson, et al. (2001). "Attention turns to naturally occuring methane seepage." EOS Transactions(82): 457.
Lake, C. H. and B. H. Toby (2011). "Rigid body refinements in GSAS/EXPGUI." Powder Diffraction **26**: S13-S21.
Larson, A. C. and R. B. Von Dreele (1994). "General Structure Analysis System (GSAS)." Los Alamos National Laboratory Report **LAUR** 86-748.
Lee, H., J. W. Lee, et al. (2005). "Tuning clathrate hydrates for hydrogen storage." Nature **434**(7034): 743-746.
Lee, H., Y. Seo, et al. (2003). "Recovering methane from solid methane hydrate with carbon dioxide." Angewandte Chemie-International Edition **42**(41): 5048-5051.
Lisgarten, N. D. and M. Blackman (1956). "The Cubic Form of Ice." Nature **178**(4523): 39-40.
Lokshin, K. A. and Y. S. Zhao (2006). "Fast synthesis method and phase diagram of hydrogen clathrate hydrate." Applied Physics Letters **88**(13).
Lokshin, K. A., Y. S. Zhao, et al. (2004). "Structure and dynamics of hydrogen molecules in the novel clathrate hydrate by high pressure neutron diffraction." Physical Review Letters **93**(12).
Makogon, Y. (1987). "Gaseous Hydrates - The Frozen Energy." Recherche **18**(192): 1192-1200.
Mao, W. L., C. A. Koh, et al. (2007). "Clathrate, hydrates under pressure." Physics Today **60**(10): 42-47.
Mao, W. L., H. K. Mao, et al. (2002). "Hydrogen clusters in clathrate hydrate." Science **297**(5590): 2247-2249.
March, A. (1932). "Mathematical theory on regulation according to the particle shape i affine deformation." Zeitschrift Fur Kristallographie **81**(3/4): 285-297.
McCallum, S. D., D. E. Riestenberg, et al. (2007). "Effect of pressure vessel size on the formation of gas hydrates." Journal of Petroleum Science and Engineering **56**(1-3): 54-64.
McCusker, L. B., R. B. Von Dreele, et al. (1999). "Rietveld refinement guidelines." Journal of Applied Crystallography **32**: 36-50.
Melnikov, V. P., A. N. Nesterov, et al. (2012). "NMR evidence of supercooled water formation during gas hydrate dissociation below the melting point of ice." Chemical Engineering Science **71**: 573-577.
Melnikov, V. P., A. N. Nesterov, et al. (2009). "Evidence of liquid water formation during methane hydrates dissociation below the ice point." Chemical Engineering Science **64**(6): 1160-1166.
Milkov, A. V. (2004). "Global estimates of hydrate-bound gas in marine sediments: how much is really out there?" Earth-Science Reviews **66**(3-4): 183-197.
Momma, K. and F. Izumi (2011). "VESTA 3 for three-dimensional visualization of crystal, volumetric and morphology data." Journal of Applied Crystallography **44**: 1272-1276.

Moridis, G. J. and E. D. Sloan (2007). "Gas production potential of disperse low-saturation hydrate accumulations in oceanic sediments." Energy Conversion and Management **48**(6): 1834-1849.
Neumann, D. A. (2006). "Neutron scattering and hydrogenous materials." Materials Today **9**(1-2): 34-41.
Nisbet, E. G. (2002). "Have sudden large releases of methane from geological reservoirs occurred since the Last Glacial Maximum, and could such releases occur again?" Philosophical Transactions of the Royal Society of London Series a-Mathematical Physical and Engineering Sciences **360**(1793): 581-607.
Ogienko, A. G., A. V. Kurnosov, et al. (2006). "Gas hydrates of argon and methane synthesized at high pressures: Composition, thermal expansion, and self-preservation." Journal of Physical Chemistry B **110**(6): 2840-2846.
Ohgaki, K., K. Takano, et al. (1996). "Methane exploitation by carbon dioxide from gas hydrates - Phase equilibria for CO2-CH4 mixed hydrate system." Journal of Chemical Engineering of Japan **29**(3): 478-483.
Ota, M., K. Morohashi, et al. (2005). "Replacement of CH4 in the hydrate by use of liquid CO2." Energy Conversion and Management **46**(11-12): 1680-1691.
Paull, C. K., W. Ussler, et al. (1991). "Is the extent of glaciation limited by marine gas-hydrates?" Geophysical Research Letters **18**(3): 432.
Priest, J. A., E. V. L. Rees, et al. (2009). "Influence of gas hydrate morphology on the seismic velocities of sands." Journal of Geophysical Research - Solid Earth **114**.
Putnis, A. (1992). An Introduction to Mineral Sciences, Cambridge University Press.
Qi, Y. X., M. Ota, et al. (2011). "Molecular dynamics simulation of replacement of CH(4) in hydrate with CO(2)." Energy Conversion and Management **52**(7): 2682-2687.
Rasmussen, R. A. and M. A. K. Khalil (1981). "Increase in the concentration of atmospheric methane." Atmospheric Environment (1967) **15**(5): 883-886.
Rietveld, H. M. (1969). "A Profile Refinement Method for Nuclear and magnetic structures." Journal of Applied Crystallography **2**: 65-&.
Ripmeester, J. A. (2000). Hydrate research - From correlations to a knowledge-based discipline - The importance of structure. Gas Hydrates: Challenges for the Future. G. D. Holder and P. R. Bishnoi. **912:** 1-16.
Ripmeester, J. A. and C. I. Ratcliffe (1998). "The diverse nature of dodecahedral cages in clathrate hydrates as revealed by Xe-129 and C-13 NMR spectroscopy: CO2 as a small-cage guest." Energy & Fuels **12**(2): 197-200.
Ruppel, C. and D. Noserale (2012) "Gas Hydrates and Climate Warming - Why a Methane Catastrophe is Unlikely." Sound Waves.

Schicks, J. M. and J. A. Ripmeester (2004). "The coexistence of two different methane hydrate phases under moderate pressure and temperature conditions: Kinetic versus thermodynamic products." Angewandte Chemie-International Edition **43**(25): 3310-3313.
Schmale, O., J. Greinert, et al. (2005). "Methane emission from high-intensity marine gas seeps in the Black Sea into the atmosphere." Geophysical Research Letters **32**(7).
Shallcross, F. V. and G. B. Carpenter (1957). "X-Ray Diffraction Study of the Cubic Phase of Ice." The Journal of Chemical Physics **26**(4): 782.
Shimaoka, K. (1960). "Electron Diffraction Study of Ice." Journal of the Physical Society of Japan **15**(1): 106-119.
Sloan, E. D. (1998). Clathrate Hydrates of Natural Gases. New York, Marcel Dekker.
Sloan, E. D. (2003). "Fundamental principles and applications of natural gas hydrates." Nature **426**(6964): 353-359.
Sloan, E. D. and C. A. Koh (2007). Clathrate Hydrates of Natural Gases, Taylor & Francis CRC Press.
Sloan, E. D. and C. A. Koh (2008). Clathrate Hydrates of Natural Gases, Taylor & Francis CRC Press.
Stackelberg, M. v. and H. R. Muller (1954). "Feste gas hydrate II: Struktur und Raumchemie." Zeitschrift Fur Elektrochemie **58**(1): 25-39.
Stern, L. A., S. Circone, et al. (2001). "Anomalous preservation of pure methane hydrate at 1 atm." Journal of Physical Chemistry B **105**(9): 1756-1762.
Stern, L. A., S. Circone, et al. (2003). "Temperature, pressure, and compositional effects on anomalous or "self" preservation of gas hydrates." Canadian Journal of Physics **81**(1-2): 271-283.
Stout, G. H. and L. H. Jensen (1989). X-ray structure determination: a practical guide, Wiley.
Strobel, T. A., C. A. Koh, et al. (2007). "Hydrogen storage properties of clathrate hydrate materials." Fluid Phase Equilibria **261**(1-2): 382-389.
Suess, E., G. Bohrmann, et al. (1999). "Flammable ice." Scientific American **281**(5): 76-83.
Sugisaki, M., H. Suga, et al. (1968). "Calorimetric Study of the Glassy State. IV. Heat Capacities of Glassy Water and Cubic Ice." Bulletin of the Chemical Society of Japan **41**(11): 2591-2599.
Sun, C. Y., W. Z. Li, et al. (2011). "Progress in Research of Gas Hydrate." Chinese Journal of Chemical Engineering **19**(1): 151-162.
Takeya, K., K. Nango, et al. (2005). "Activation energy of methyl radical decay in methane hydrate." Journal of Physical Chemistry B **109**(44): 21086-21088.
Takeya, S., T. Ebinuma, et al. (2002). "Self-preservation effect and dissociation rates of CH4 hydrate." Journal of Crystal Growth **237**: 379-382.
Takeya, S. and J. A. Ripmeester (2008). "Dissociation behavior of clathrate hydrates to ice and dependence on guest molecules." Angewandte Chemie-International Edition **47**(7): 1276-1279.

Takeya, S., W. Shimada, et al. (2001). "In situ X-ray diffraction measurements of the self-preservation effect of CH4 hydrate." Journal of Physical Chemistry A **105**(42): 9756-9759.
Takeya, S., T. Uchida, et al. (2005). "Particle size effect of CH4 hydrate for self-preservation." Chemical Engineering Science **60**(5): 1383-1387.
Takeya, S., K. A. Udachin, et al. (2010). "Direct Space Methods for Powder X-ray Diffraction for Guest-Host Materials: Applications to Cage Occupancies and Guest Distributions in Clathrate Hydrates." Journal of the American Chemical Society **132**(2): 524-531.
Thomas, D. J., J. C. Zachos, et al. (2002). "Warming the fuel for the fire: Evidence for the thermal dissociation of methane hydrate during the Paleocene-Eocene thermal maximum." Geology **30**(12): 1067-1070.
Toby, B. H. (2001). "EXPGUI, a graphical user interface for GSAS." Journal of Applied Crystallography **34**: 210-213.
Tse, J. S., C. I. Ratcliffe, et al. (1997). "Rotational and translational motions of trapped methane. Incoherent inelastic neutron scattering of methane hydrate." Journal of Physical Chemistry A **101**(25): 4491-4495.
Tsimpanogiannis, I. N. and P. C. Lichtner (2007). "Parametric study of methane hydrate dissociation in oceanic sediments driven by thermal stimulation." Journal of Petroleum Science and Engineering **56**(1-3): 165-175.
Ullerich, J. W., M. S. Selim, et al. (1987). "Theory and Measurement of Hydrate Dissociation." Aiche Journal **33**(5): 747-752.
Van der Waals, J. H. and J. C. Platteeuw (1959). "Clathrate Solutions." Advances in Chemical Physics **2**: 1-57.
Westbrook, G. K., K. E. Thatcher, et al. (2009). "Escape of methane gas from the seabed along the West Spitsbergen continental margin." Geophysical Research Letters **36**.
Yakushev, V. S. and V. A. Istomin (1992). Gas-Hydrate, Self-Preservation Effect. Physics and Chemistry of Ice. Japan, Hokkaido University Press.
Yezdimer, E. M., P. T. Cummings, et al. (2002). "Determination of the Gibbs free energy of gas replacement in SI clathrate hydrates by molecular simulation." Journal of Physical Chemistry A **106**(34): 7982-7987.
Young, R. A. (1995). The Rietveld Method, Oxford University Press.
Yuan, Q., C. Y. Sun, et al. (2012). "Recovery of methane from hydrate reservoir with gaseous carbon dioxide using a three-dimensional middle-size reactor." Energy **40**(1): 47-58.
Zhao, J. F., K. Xu, et al. (2012). "A Review on Research on Replacement of CH4 in Natural Gas Hydrates by Use of CO2." Energies **5**(2): 399-419.

APPENDIX

Figures

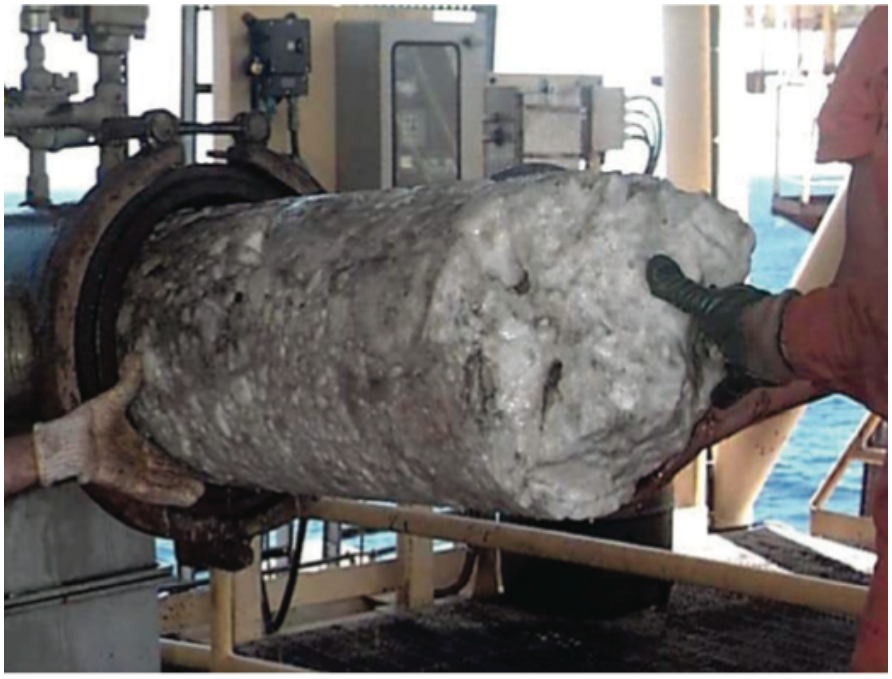

Figure A - 1. Pipeline hydrate plug

A subsea gas pipeline has been plugged by hydrate formation and recovered from a slug catcher off the coast of Brazil (courtesy of Petrobras via Mao (Mao, Koh et al. 2007)).

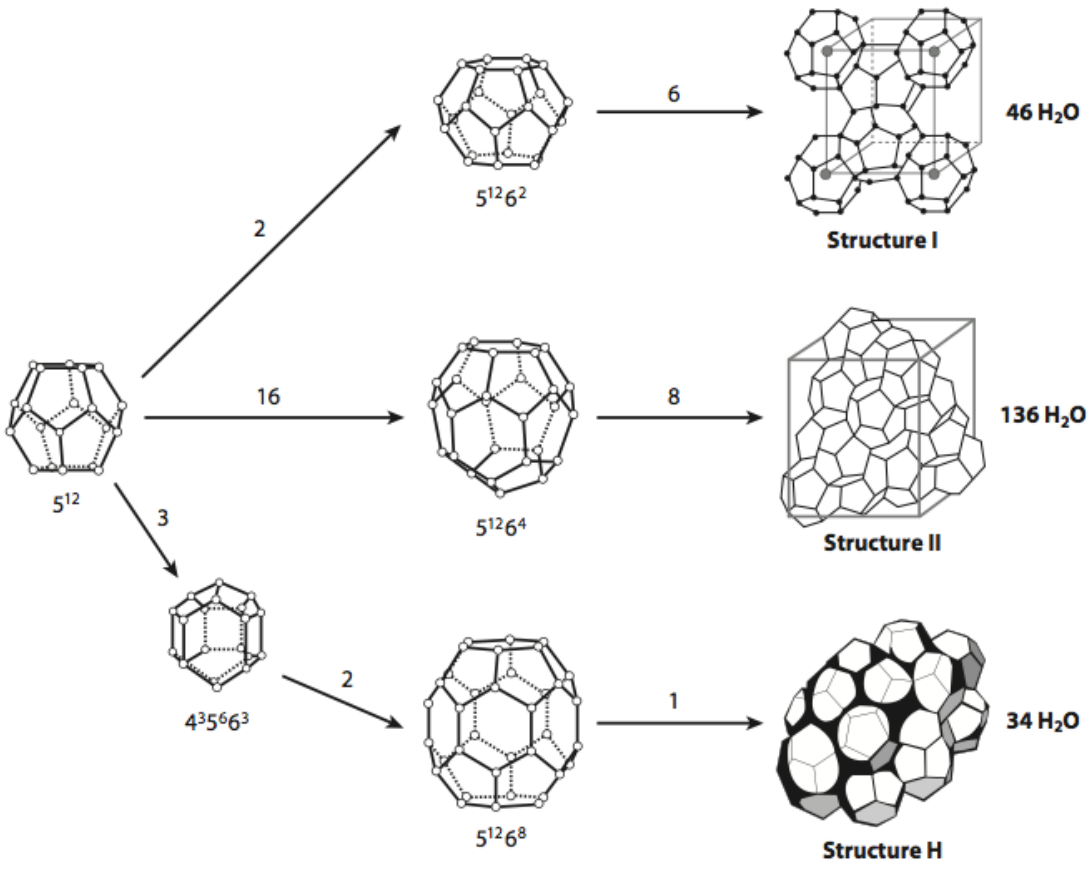

Figure A - 2. Cage structures for gas hydrates

Top row shows cages for sI, middle is sII and bottom is sH (courtesy of Koh (Koh, Sloan et al. 2011)). sI has two small cages (5^{12}) and six large cages ($5^{12}6^2$) made from 46 H_2O molecules per unit cell. sII has sixteen small cages (5^{12}) and eight large cages ($5^{12}6^4$) made from 136 H_2O molecules per unit cell. Both sI and sII crystallize in the cubic crystal system with lattice parameters of approximately 12 and 17 Å, respectively. sH has three (5^{12}), two ($4^3 5^6 6^3$) and one ($5^{12}6^8$) from 34 H_2O molecules, and crystallizes in the hexagonal crystal system.

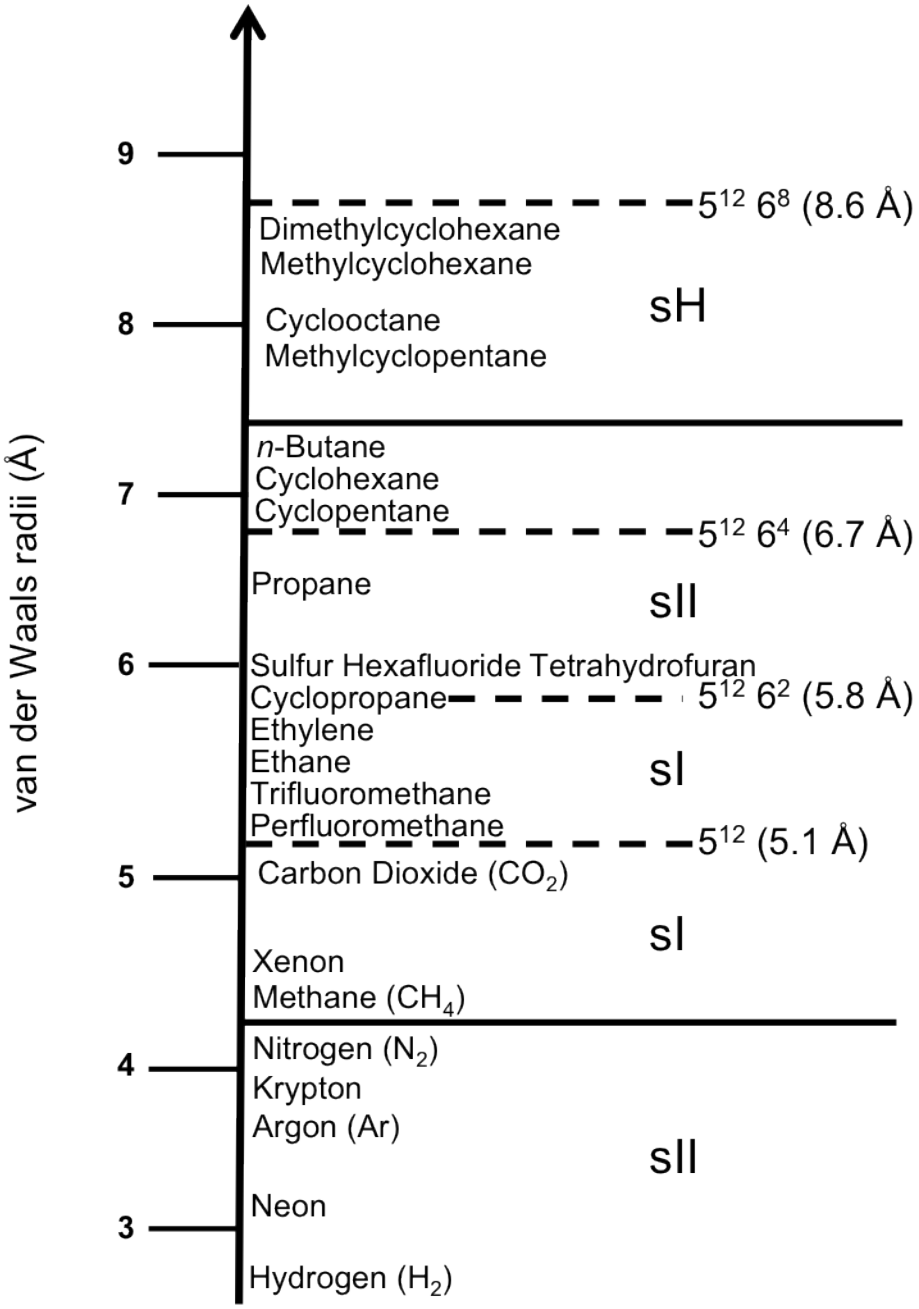

Figure A - 3. Hydrate guest size

Hydrate formers and how their size relates to the internal free volume of the various cages for sI, sII, and sH (adapted from Sloan (Sloan and Koh 2008)).

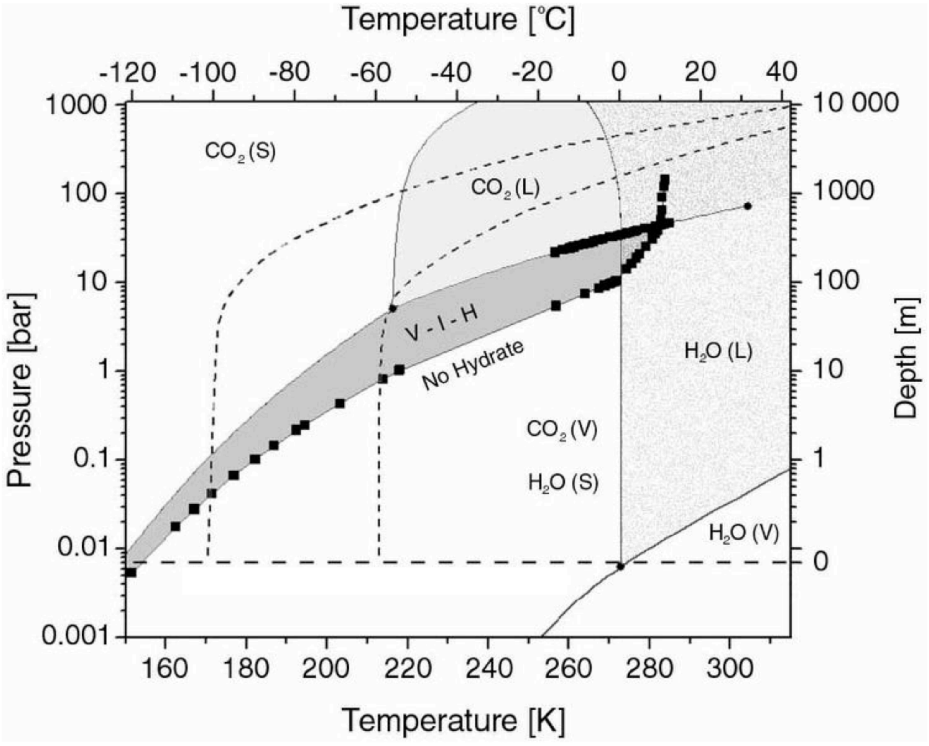

Figure A - 4. CO_2 hydrate phase diagram

The black diamonds represent experimental data reported by Sloan. The phase boundaries for water are just guidelines (courtesy of Genov (Genov 2005)).

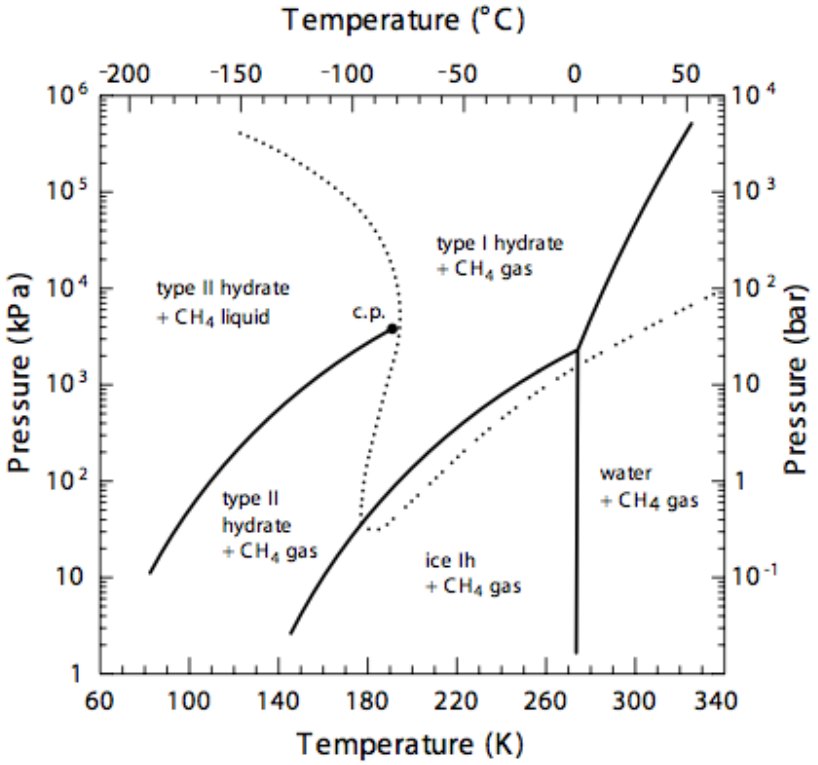

Figure A - 5. CH_4 hydrate phase diagram

Water, ice, and CH_4 hydrate phase boundaries are represented by bold lines. Calculated phase boundaries for sI and sII CH_4 hydrate are shown with dotted lines (courtesy of Kuhs (Kuhs and Hansen 2006)).

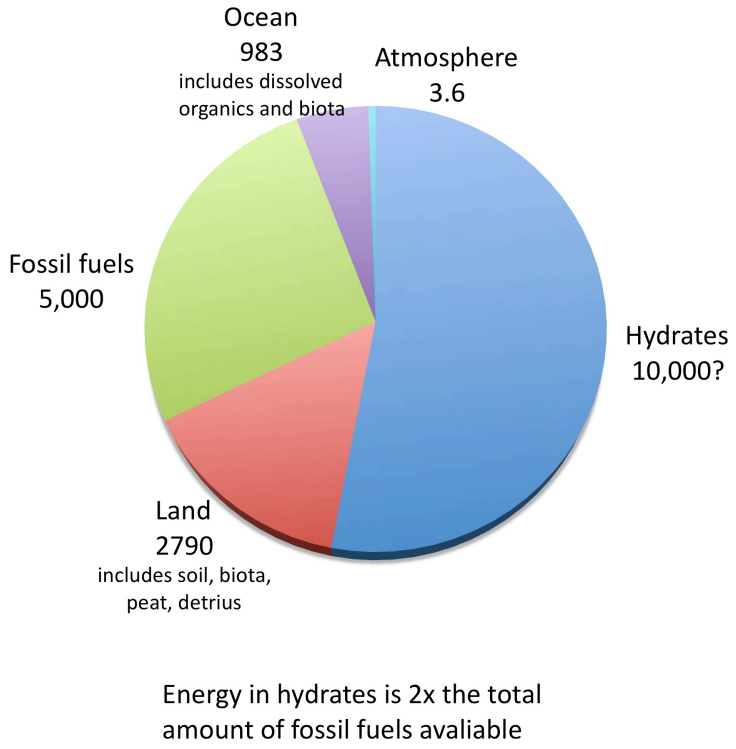

Figure A - 6. Energy reserves

Gigaton (10^{15} ton) estimates of energy reserves are shown as they compare to hydrates (adapted from Koh (Koh, Sloan et al. 2011)).

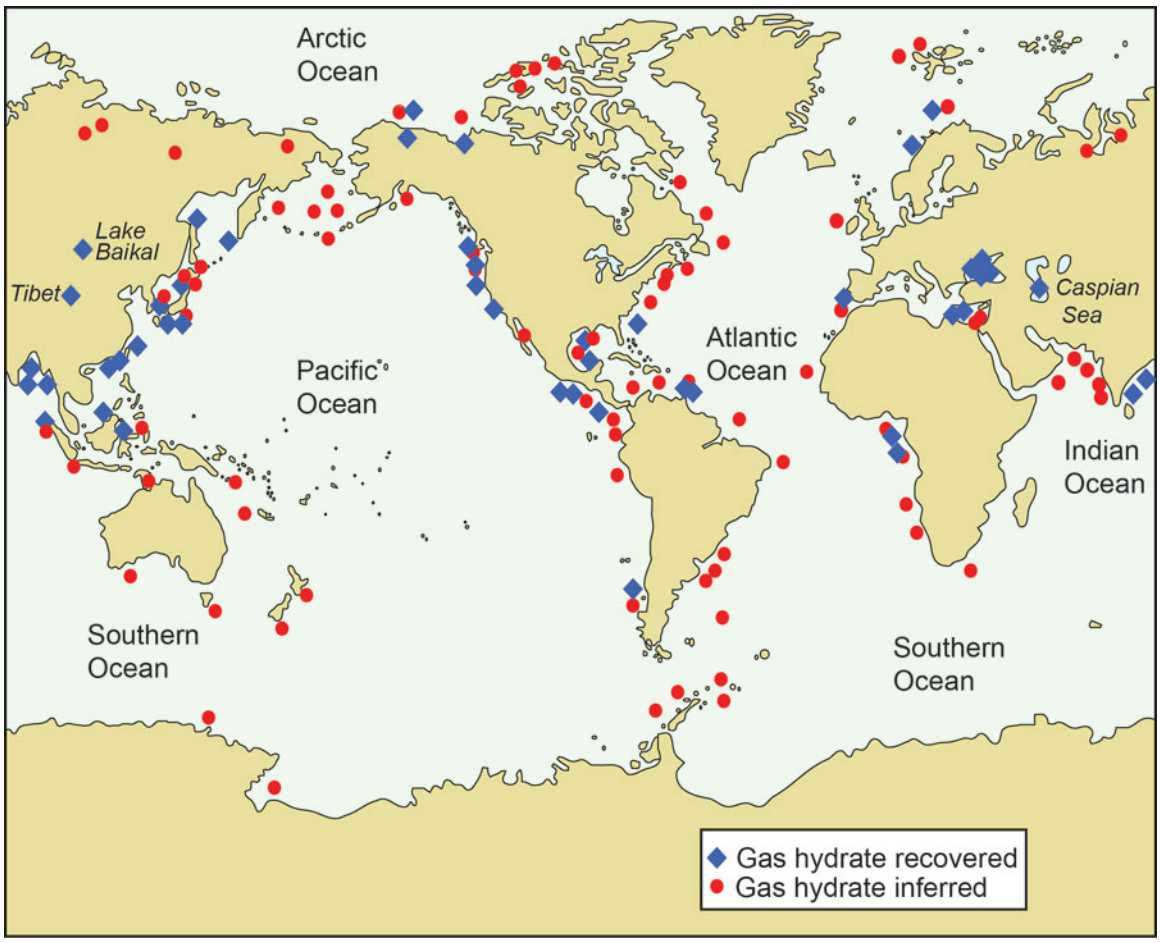

Figure A - 7. Global hydrate deposits

Blue diamonds indicate areas where hydrates have been recovered. Red dots indicate areas where geophysical data suggests hydrates are present (courtesy of Ruppel (Ruppel and Noserale 2012)).

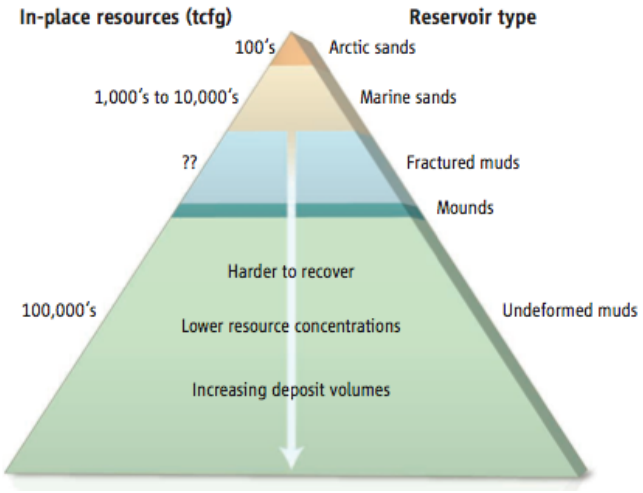

Figure A - 8. Hydrate reserve estimates

The amounts of hydrates and their location are shown in this pyramid. The most accessible reserves are shown at the top (courtesy of Boswell (Boswell 2009)).

Figure A - 9. Experimental aids

Ice trays used to form thin layers of ice I_h. 500 μm sieves to ensure uniform particle size of ice I_h for hydrate synthesis.

Figure A - 10. Parr vessel

A 450 mL pressure vessel, used for hydrate synthesis, with a 600 psi gauge (1000 psi rupture disc). Black collars on top and bottom were added for use with a tumbler.

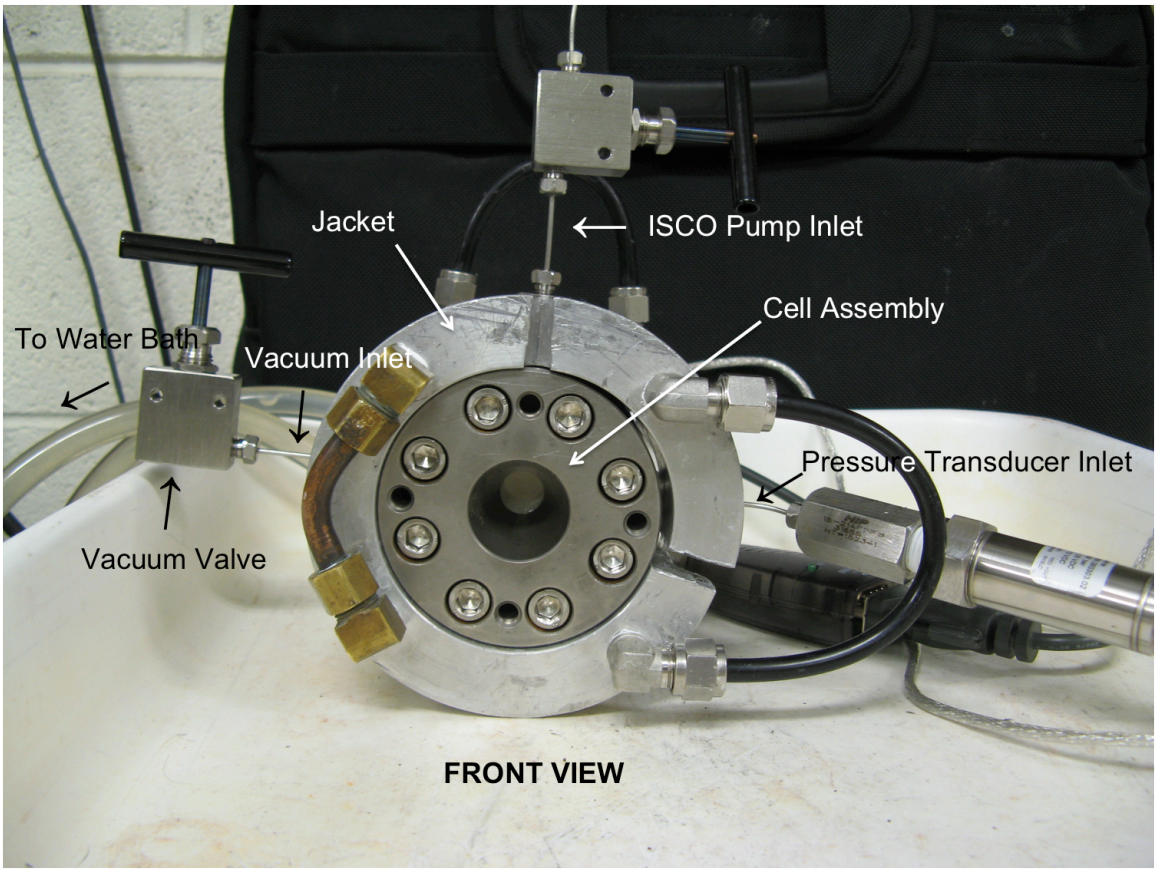

Figure A - 11. McHugh cell

Mark A. McHugh of Virginia Commonwealth University designed this pressure cell for small angle neutron scattering geometry. It is equipped with sapphire windows for neutron transmission, and has the ability for 4 inlet ports. As shown here, only three are utilized: pressure transducer, syringe pump, and vacuum line. The outside jacket is Al; it is connected to a cooling bath for temperature control.

Figure A - 12. Hydrate dissociation

Hydrate was first observed in the cell with a pressure of 5.2 MPa and temperature of 4 °C. The temperature was raised at 1 °C/hr to 8 °C. The pressure rose to 7.8 MPa. The temperature was then raised from 8 to 12 °C at a rate of 1 ° per 15 minutes. The pressure leveled out at 9.6 MPa, and total dissociation of hydrate was achieved. Dissociation began at t = 0 s shown when the temperature equilibrated at 12 °C, and was mostly complete at t = 35 s. Gas bubble formation started at t = 25 s and was prominent at t = 30 s. The temperature was turned down directly to 6 °C, and hydrate successfully reformed within 30 minutes.

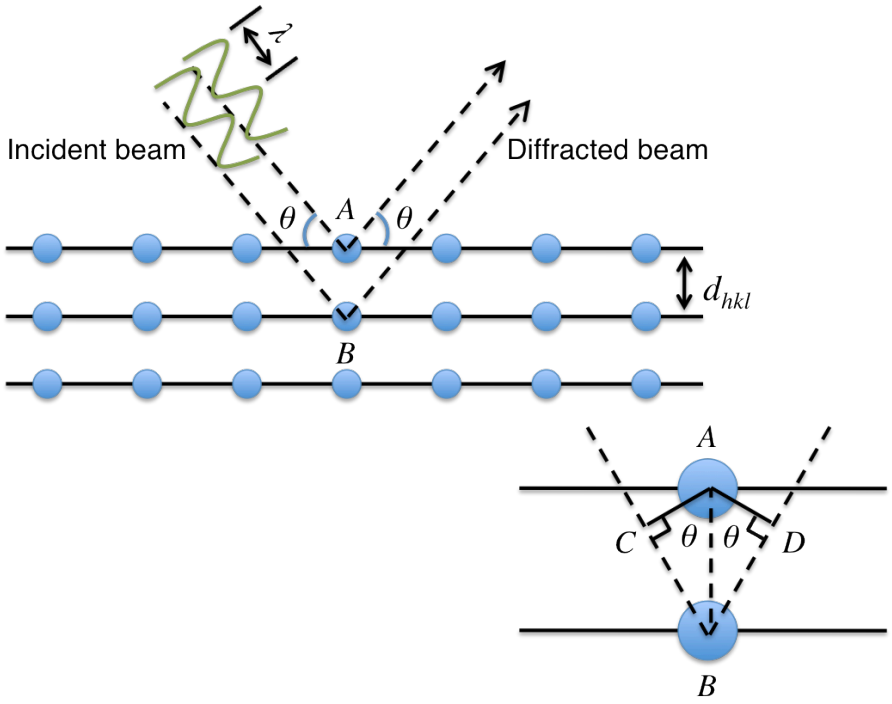

Figure A - 13. Diffraction of x-rays by atomic planes

Incoming radiation diffracts from planes of atoms demonstrating the basis of Bragg's law, $n\lambda = 2d\sin\theta$, which relates the wavelength of the radiation to the inter-planar spacing and angle of diffraction.

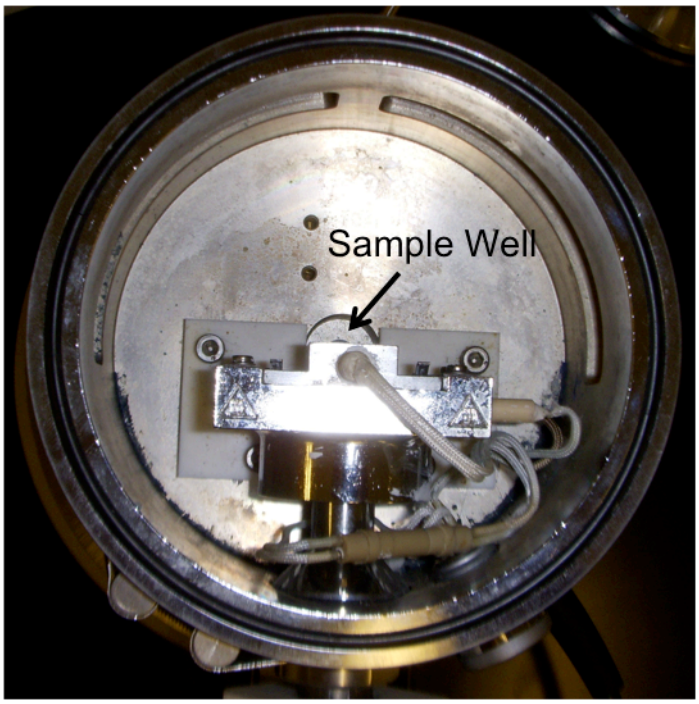

Figure A - 14. LTXRD environmental chamber

Anton Parr TTK450 environmental chamber used for LTXRD measurements on a PANalytical X'Pert Pro multi-purpose diffractometer. The sample well is labeled. When in use, liquid nitrogen flows through the stage to maintain the proper temperature.

Figure A - 15. V can

V, with a bound coherent neutron scattering length of 0.384 fm, is basically transparent to neutrons and only marginally contributes to the diffraction pattern (data is subsequently corrected for this). This is a 10 mm OD V can used to collect hydrate samples for Debye – Scherrer geometry. The vapor is a result of storage in liquid nitrogen.

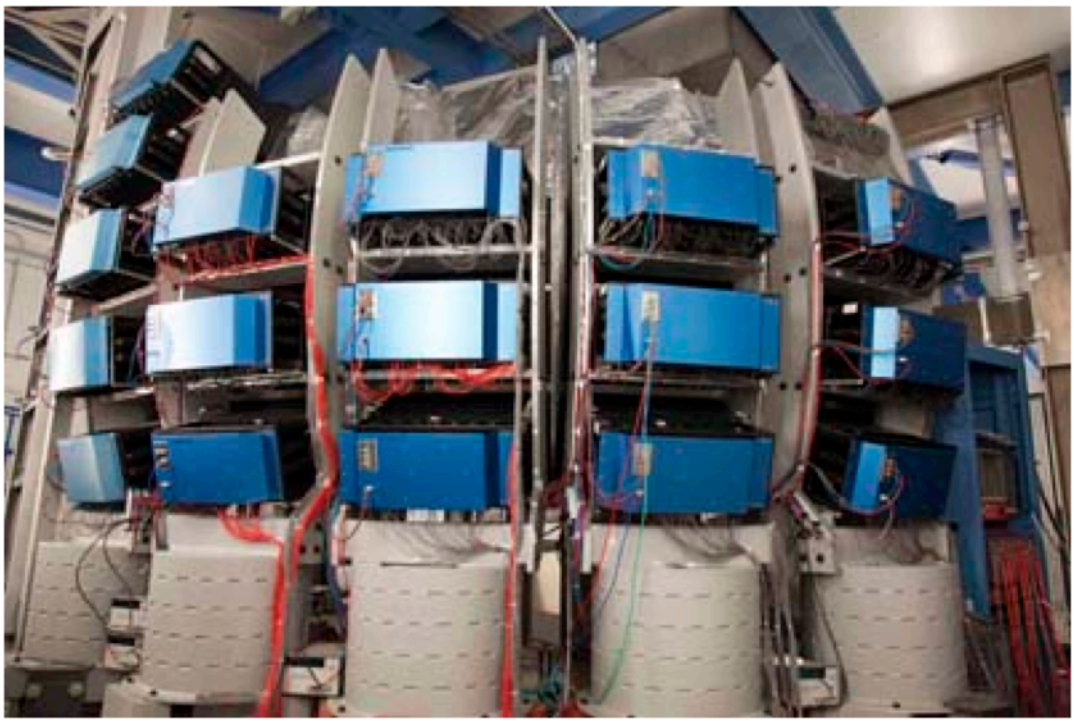

Figure A - 16. POWGEN detector bank

Detectors for the POWGEN instrument at Spallation Neutron Source, Oak Ridge National Laboratory. They are set-up for data collection in the Debye – Scherrer geometry.

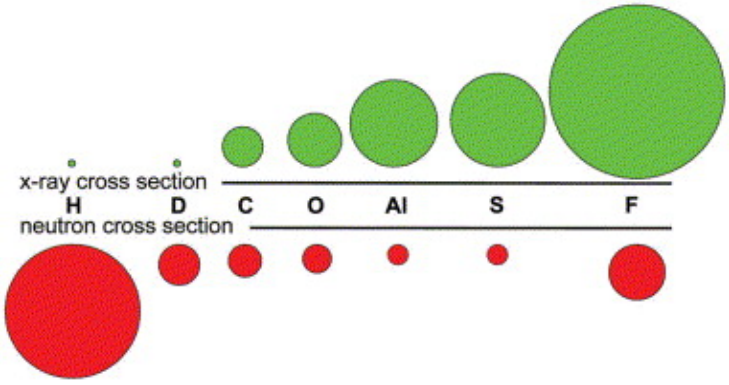

Figure A - 17. Cross section comparison

A graphical representation of how the relative scattering cross section of neutrons compares to that of x-rays. Specifically, this shows that H and D can be more easily identified through neutron diffraction (courtesy of Muhammad Arif via Neumann (Neumann 2006)).

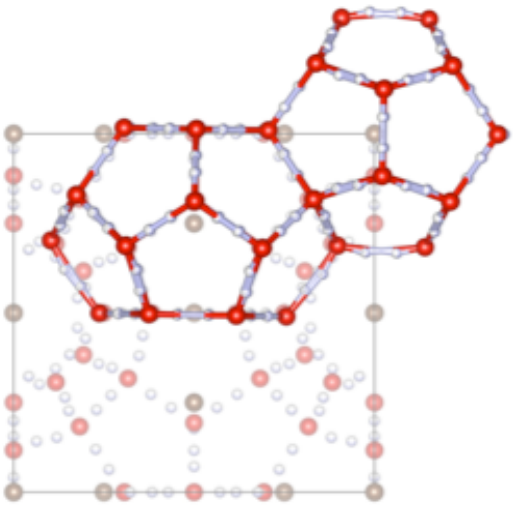

Figure A - 18. Large and small cage of sI placed in the unit cell

Two polyhedral cages (large cage on left, small cage on right) defined by the hydrogen bonded water network in sI hydrate as compared to their location in the unit cell. The vertices are the locations of the oxygen atoms (red), the edges are hydrogen sites (white) randomly half occupied, and the centers of the cages contain one single carbon atom (brown) to indicate the gas placement.

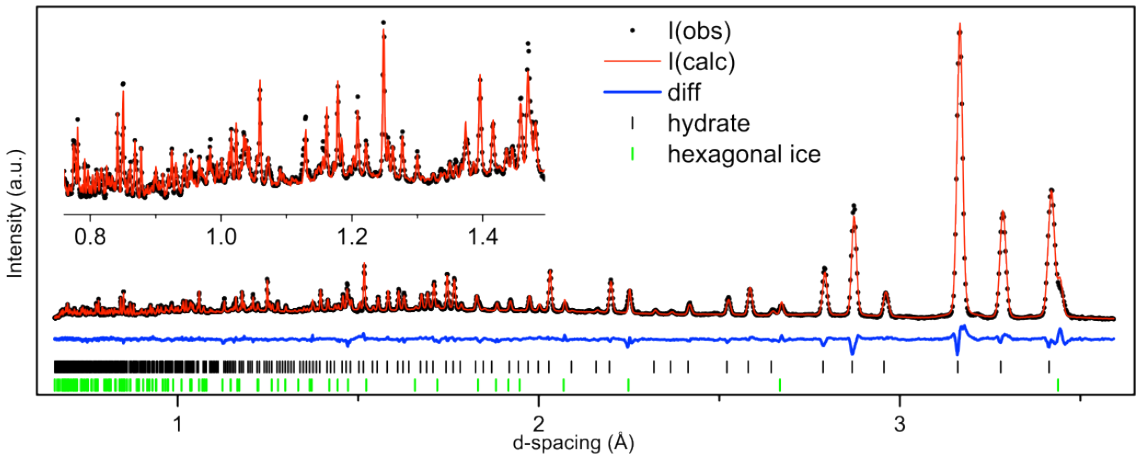

Figure A - 19. Powder pattern for 50% CH_4 nominal sample

Neutron observed, calculated, and difference powder diffraction patterns for 50% CO_2/50% CH_4 feed gas sample. 0.7 – 1.5 Å has been enlarged to show the resolvability of the low d range.

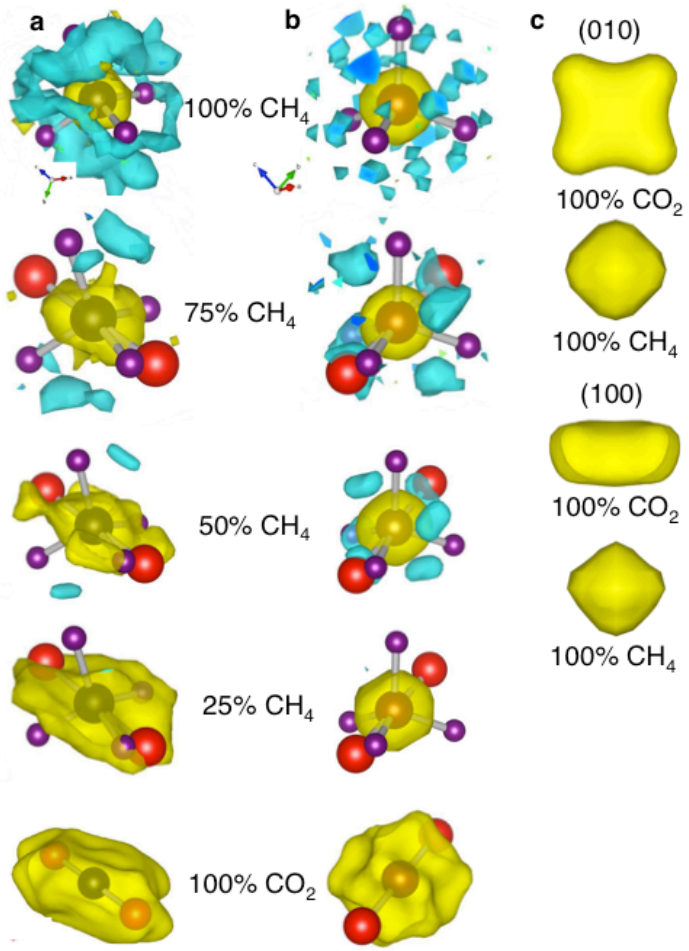

Figure A - 20. Nuclear scattering densities

Graphic displays of nuclear densities of guest gas molecules as determined by Fourier difference analysis of CO_2/CH_4 gas hydrate. Large cages depicted on the left (a) and small cages on the right (b). The isosurface level is 1.5 fm/Å^3 for last four samples (nominal compositions of 75% CH_4, 50% CH_4, 25% CH_4, and 100% CO_2), and 2.2 fm/Å^3 for the nominal composition of 100% CH_4 (to eliminate extra noise created by high incoherent scattering of H_2). Positive nuclear scattering (oxygen and carbon) is shown in yellow, negative (hydrogen) in blue. A single CO_2 and/or CH_4 molecule has been superimposed to give a spatial sense of the molecule compared to the observed nuclear density. Energy maxima determined from the nuclear density for the large cage (c) with isosurface level 3 fm/Å^3; CO_2 top, CH_4 bottom, shown along both the (010) and (100) projection vectors in the large cage to demonstrate the extent of the anisotropy of CO_2 on this site.

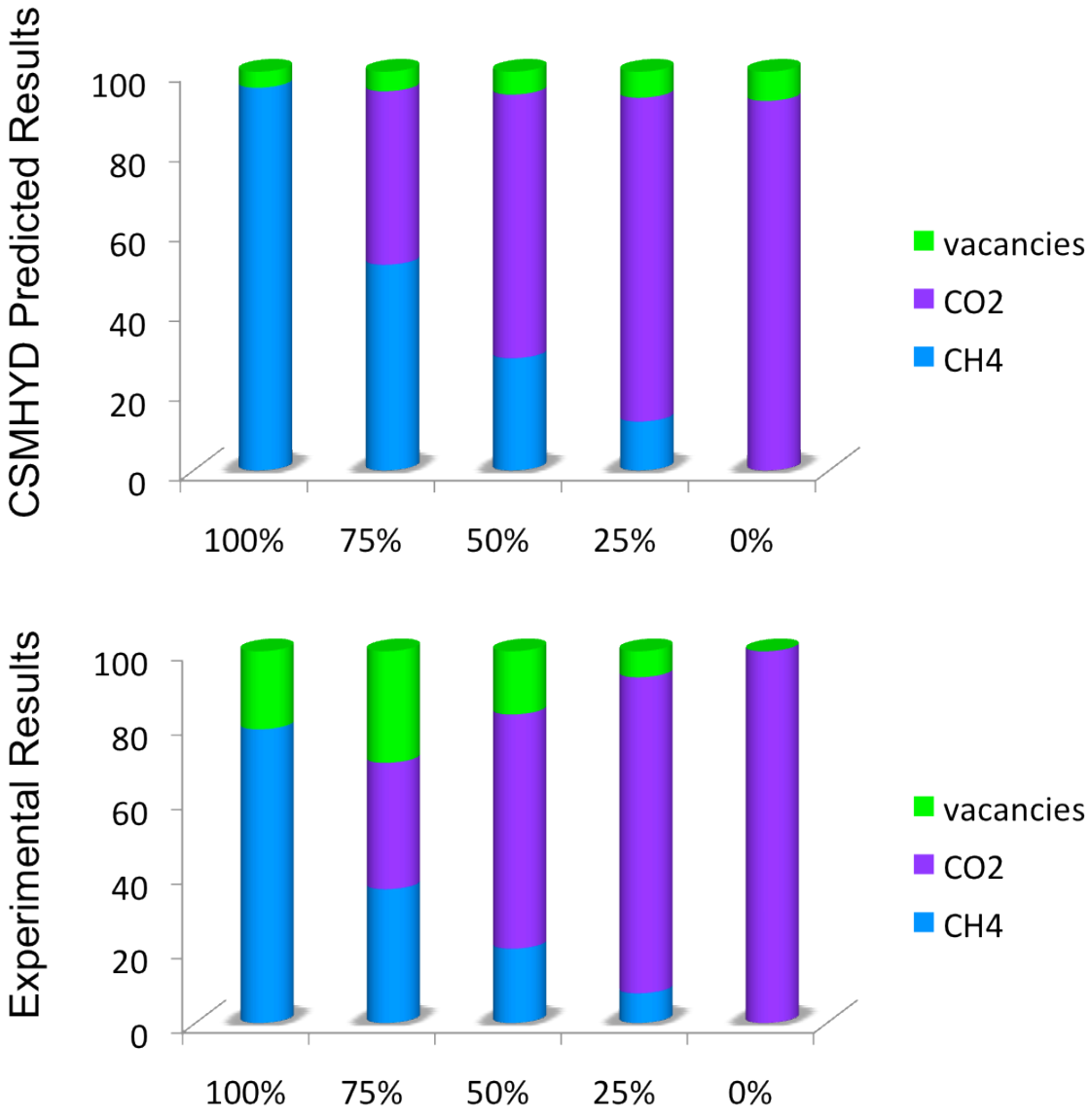

Figure A - 21. Experimental vs. CSMHYD predicted occupancy results

CSMHYD (Sloan 1998) was used to predict the results of the cage occupancies based on the same experimental results (top). The experimental results from Rietveld refinement (bottom) are compared to those results. The y-axis represents the cage occupancy of either CH_4, CO_2, or vacancies, and the x-axis represents the CH_4 nominal feed gas amount.

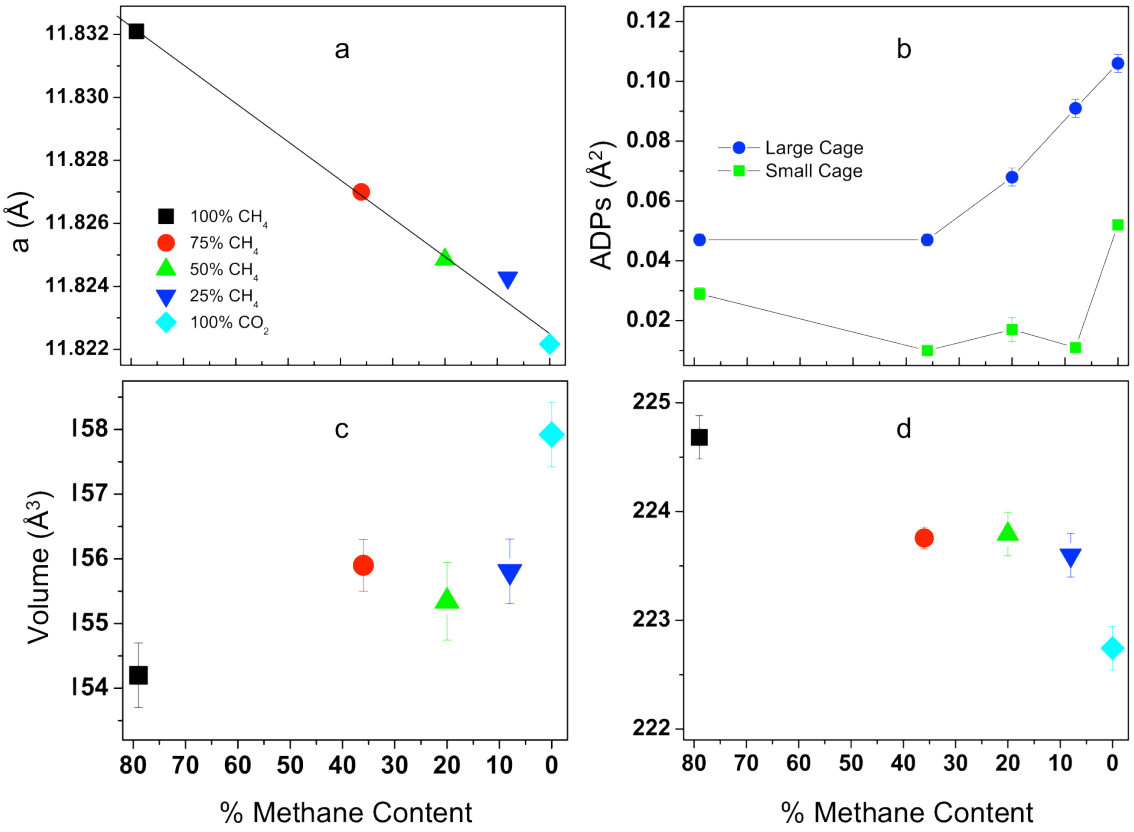

Figure A - 22. Lattice parameters, ADPs, cell volumes, and density

Refined lattice parameters (a) and refined atomic displacement parameters (b). Volumes of the small cages (c) and large cages (d) calculated from the refined atomic coordinates. The top legend denotes the sample names as they correspond to the nominal feed gas composition.

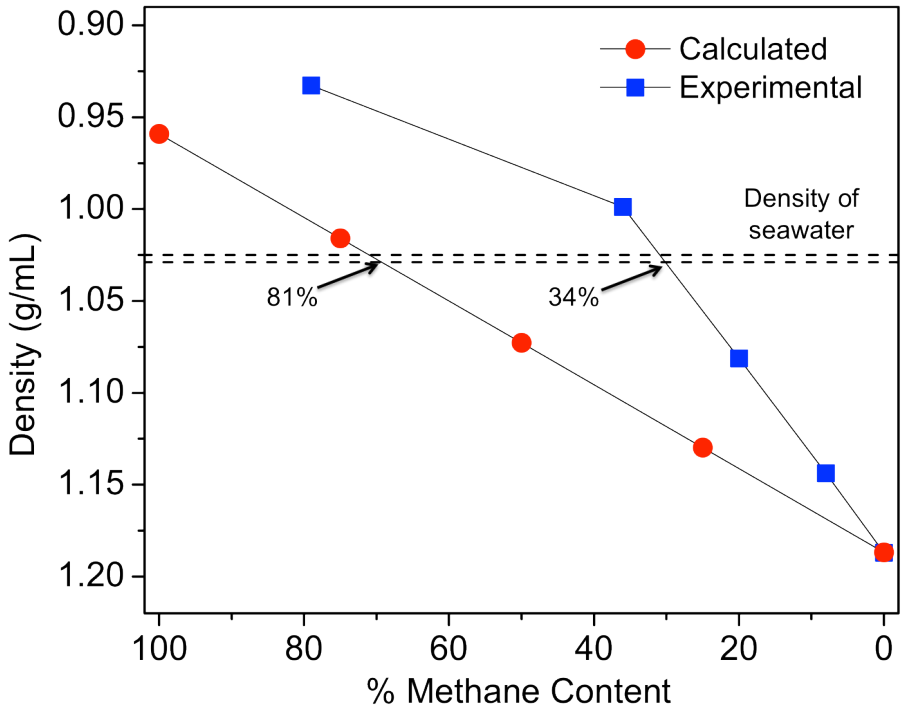

Figure A - 23. Density of mixed hydrates

Experimental densities determined from the refined occupancies and calculated densities for the nominal compositions (e). The calculated curve is theoretically fully occupied based on feed gas. The pure CO_2 and CH_4 data points are calculated using published lattice constants, where the mixed lattice constants are the refined constants from this study. The deviation between the experimental and calculated is likely driven by vacancies.

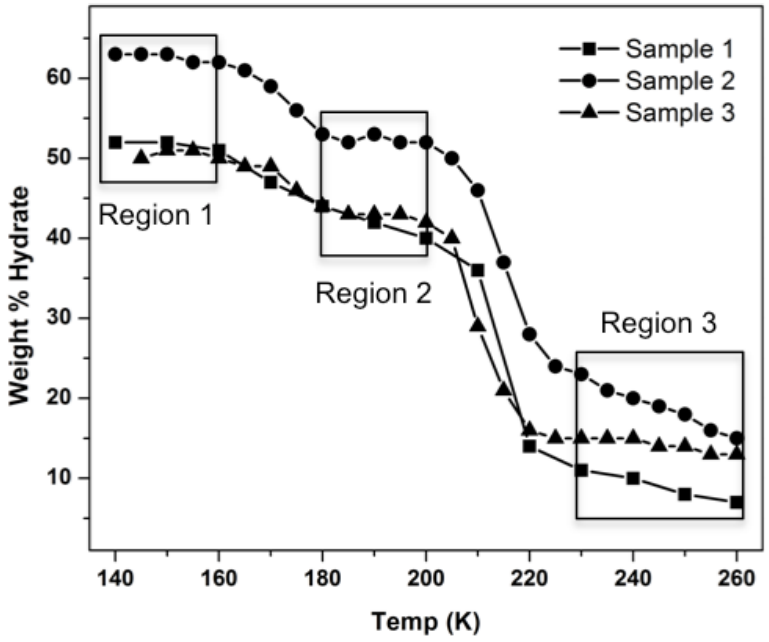

Figure A - 24. Temperature dependent decomposition

Hydrate decomposition curves of three nominally similar samples decomposed from 140 − 260 K, showing three regions of slower decomposition. An isochronal annealing procedure was used, wherein the sample was held for 10 minutes per temperature.

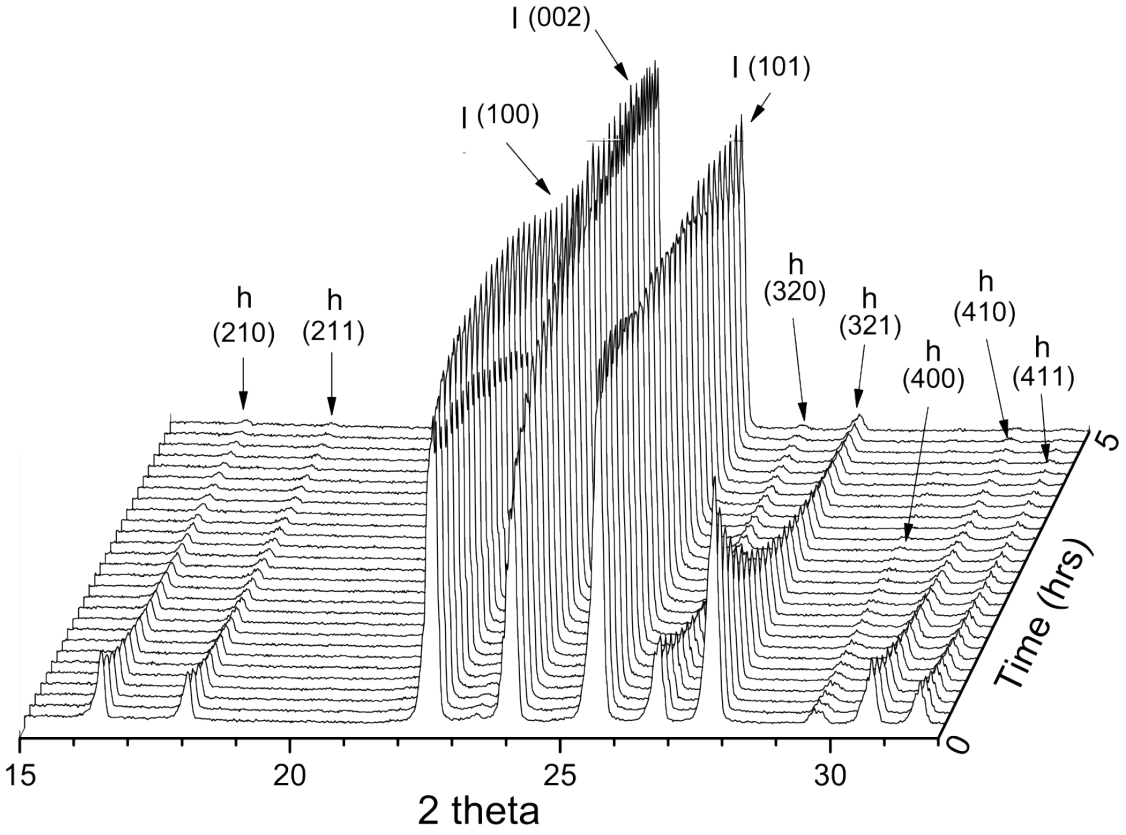

Figure A - 25. Waterfall plot of isothermal decomposition at 250K

LTXRD data collected isothermally every 10 minutes over ~7 hrs at 250 K on S1. Hydrate peaks were diminishing (h) as ice I_h peaks (I) were intensifying.

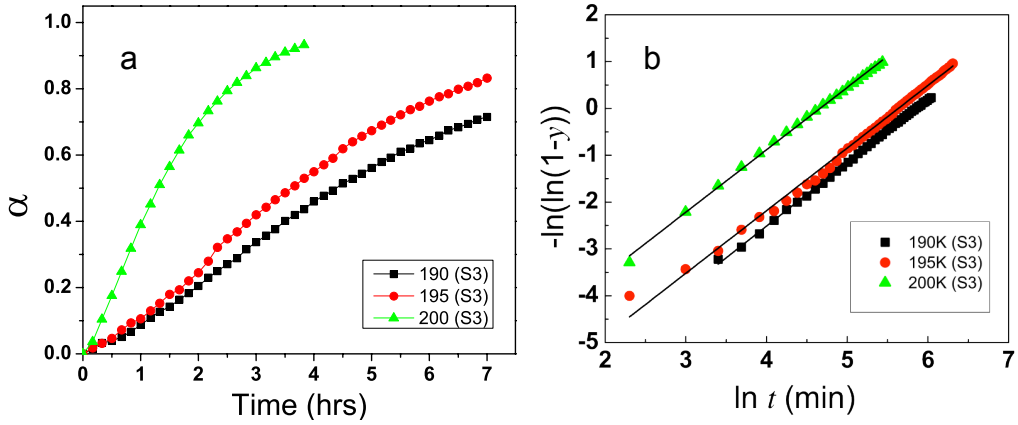

Figure A - 26. Avrami plots for Region 2

Ice phase fraction plots (a) of decomposing hydrate, for isothermal scans at 190, 195, and 200 K, for S3. Where α is the weight percent of the converted phase and t is time. Avrami plots (b) of ln(−ln(1-α)) vs. ln t. The resulting slopes, n, are in the range 1.33 ≤ n ≤ 1.36.

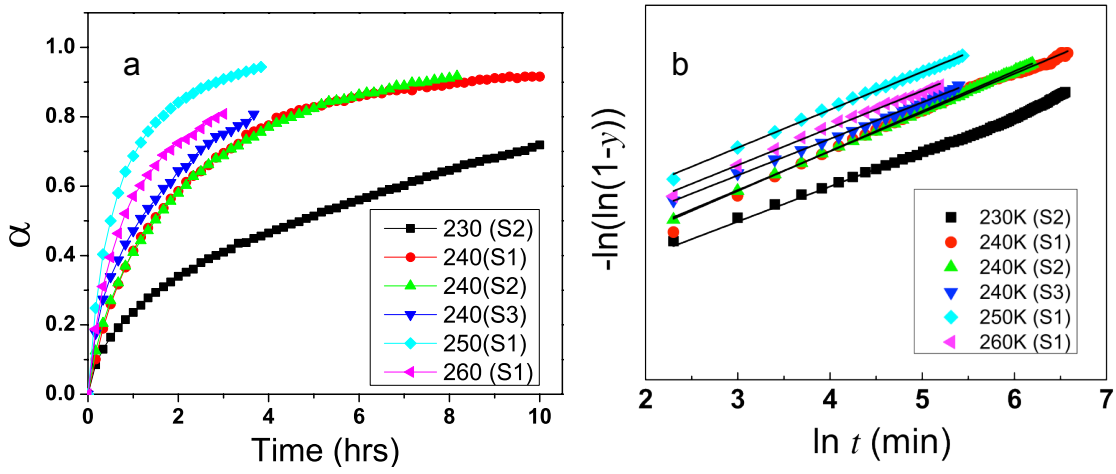

Figure A - 27. Avrami plots for Region 3

Ice phase fraction plots (a) of decomposing hydrate, for isothermal scans at 230 K (from data collected on S2), 240 K (from data collected on S1, S2, and S3), 250 K (from data collected on S1) and 260 K (from data collected on S1). Where α is the weight percent of the converted phase and t is time. Avrami plots (b) of $\ln(-\ln(1-\alpha))$ vs. $\ln t$. Avrami plots for The resulting slopes, n, are in the range $0.59 \leq n \leq 0.75$.

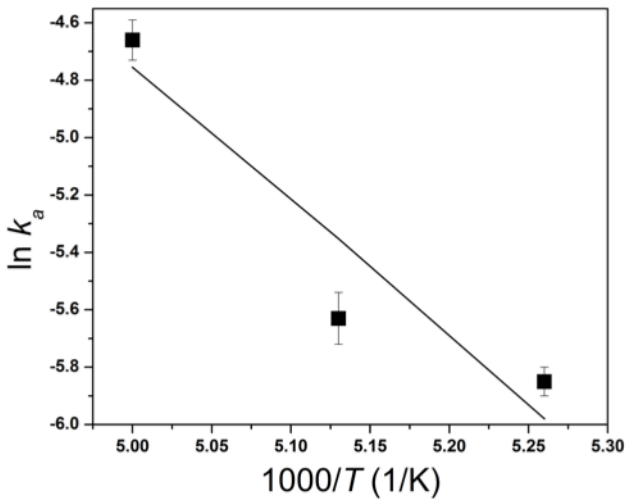

Figure A - 28. Arrhenius plot for region 2

Arrhenius plot (each point is a k_a determined by each sample from the Avrami plot) for the 180 – 200 K temperature region, slope = $-E_a/R$ therefore with slope = −5, E_a = 42 kJ/mol.

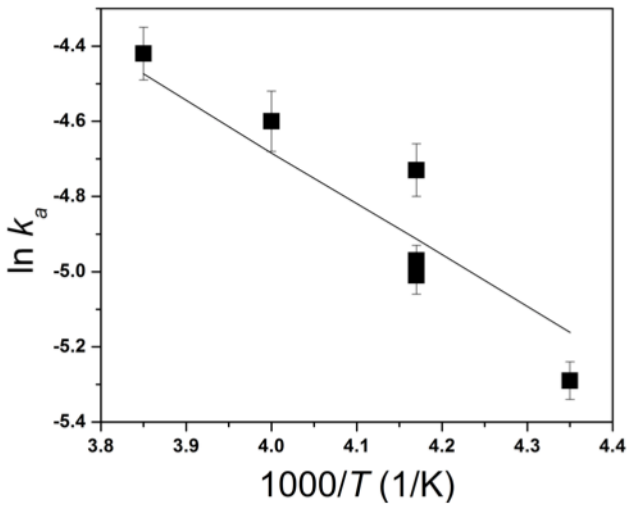

Figure A - 29. Arrhenius plot for region 3

Arrhenius plot (each point is a k_a determined by each sample from the Avrami plot) for the >240 K temperature region, slope = $-E_a/R$ therefore with slope = −2.6, E_a = 22 kJ/mol.

Tables

Table A - 1. Experimental results

Experimental information for neutron powder data collected on five hydrate samples with nominal gas amounts of 100%CH_4, 75%CH_4/25%CO_2, 50%CH_4/50%CO_2, 25%CH_4/75%CO_2, and 100%CO_2.

Refined Chemical Formula	0.79(CH_4) 5.75H_2O	0.36(CH_4)0.34(CO_2) 5.75H_2O	0.2(CH_4)0.63(CO_2) 5.75H_2O	0.08(CH_4)0.85(CO_2) 5.75H_2O	(CO_2) 5.75H_2O
Crystal system	cubic	cubic	cubic	cubic	cubic
Space group	$Pm\bar{3}n$	$Pm\bar{3}n$	$Pm\bar{3}n$	$Pm\bar{3}n$	$Pm\bar{3}n$
a (Å)	11.8321(2)*	11.8270(1)*	11.8249(2)*	11.8243(2)*	11.8222(3)*
Volume (Å^3)	1656.48	1654.34	1653.44	1653.19	1652.31
ρ_{calc} (g/cm^3)	0.93	1.00	1.08	1.14	1.19
Temp(K)	10	10	10	10	10
Phases	97% hydrate 3% ice I_h	90% hydrate 10% ice I_h	92% hydrate 8% ice I_h	90% hydrate 7% ice I_h, 3% N_2	99% hydrate 1% ice I_h
Geometry	Debye Scherrer	Debye Scherrer	Debye Scherrer	Debye Scherrer	Debye Scherrer
Variables	36	47	47	36	47

*Estimated standard deviations are reported as 3σ

Table A - 2. Rietveld results

Crystallographic goodness of fit information for neutron powder data collected on five hydrate samples with nominal gas amounts of 100%CH_4, 75%CH_4/25%CO_2, 50%CH_4/50%CO_2, 25%CH_4/75%CO_2, and 100%CO_2.

	$0.79(CH_4)\ 5.75H_2O$		$0.36(CH_4)0.34(CO_2)\ 5.75H_2O$	
Center wavelength	1.333	2.665	1.333	2.665
d-spacing range	0.57-3.59	1.23-6.16	0.66-3.59	1.15-6.16
R_p	0.009	0.011	0.022	0.032
R_{wp}	0.010	0.012	0.022	0.032
R_{exp}	0.002	0.003	0.003	0.004
χ^2	5.72	3.81	7.10	7.69
Combined R_p	0.010		0.028	
Combined R_{wp}	0.011		0.026	
Variables	36		47	

	$0.2(CH_4)0.63(CO_2)\ 5.75H_2O$		$0.05(CH_4)0.85(CO_2)\ 5.75H_2O$	
Center wavelength	1.333	2.665	1.333	2.665
d-spacing range	0.66-3.59	1.15-6.16	0.57-3.59	1.23-6.16
R_p	0.025	0.034	0.009	0.011
R_{wp}	0.024	0.035	0.010	0.012
R_{exp}	0.003	0.004	0.002	0.003
χ^2	9.38	8.16	5.72	3.81
Combined R_p	0.030		0.010	
Combined R_{wp}	0.028		0.011	
Variables	47		36	

	$(CO_2)\ 5.75H_2O$	
Center wavelength	1.333	2.665
d-spacing range	0.66-3.59	1.15-6.16
R_p	0.022	0.032
R_{wp}	0.022	0.032
R_{exp}	0.003	0.004
χ^2	7.10	7.69
Combined R_p	0.028	
Combined R_{wp}	0.026	
Variables	47	

Table A - 3. Cage occupancies and occupants

Refined cage occupancies are shown for each molecule and each cage. Those numbers are applied to the 2 SCs and 6 LCs to give the percent of each gas found. The final column shows the percentage of all cages filled.

Target	Large Cage Occ.		Small Cage Occ.		Content %		Vacancies	% Cages
Composition	CH_4	CO_2	CH_4	CO_2	CH_4	CO_2	%	Full
100% CH_4	0.73(3)	-	0.93(5)	-	79(4)	-	21	79(4)
75% CH_4	0.28(2)	0.42(1)	0.59(3)	0.09(2)	36(2)	34(1)	30	70(3)
50% CH_4	0.08(3)	0.77(1)	0.54(4)	0.21(2)	20(3)	63(1)	17	83(5)
25% CH_4	0.00(2)	0.98(2)	0.33(4)	0.47(3)	8(3)	85(2)	7	94(5)
0% CH_4	-	1.00(6)	-	1.00(4)	-	100(6)	0	100(6)

Table A - 4. Avrami constants

Avrami constants for each temperature and sample within R2 (180 – 200 K) and R3 (240 – 260 K). Assuming an instantaneous nucleation rather than sporadic, and a diffusion controlled process rather than phase boundary, the n values suggest the following crystal growths. The similar n values within the regions suggest the same growth dimensionality is occurring, just as the different n values between the regions suggest different growths.

Region	Sample	Temp (K)	n	Crystal Growth	$k_a(s^{-1})$
2	3	190	1.36	2D	0.003
2	3	195	1.33	2D	0.004
2	3	200	1.33	2D	0.009
3	1	230	0.59	1D	0.005
3	1	240	0.72	1D	0.006
3	2	240	0.75	1D	0.007
3	3	240	0.68	1D	0.009
3	1	250	0.71	1D	0.003
3	1	260	0.69	1D	0.012

VITA

Susan Michelle Everett was born in Morristown, TN to parents Lloyd and Barbara Turner. She is the younger sibling of Mark Turner. She spent the greater part of her schooling in Kingston, TN. She attended Kingston Elementary, Cherokee Middle, and graduated from Roane County High School in the top ten of her class. On scholarship, she continued her education with an Associate of Science degree in Mathematics from Roane State Community College, Harriman, TN, May 1992, and a Bachelor of Science degree in both Mathematics and Latin from The University of Tennessee, Knoxville, May 1995. After 11 years in the workplace, she returned to UTK in order to pursue an engineering degree. After starting in Aerospace Engineering, Michelle moved into the graduate program in Materials Science and Engineering through a National Science Foundation program, STAIR, Sustainable Technology through Advanced Interdisciplinary Research, as an IGERT Trainee (Integrative Graduate Education and Research Traineeship). She completed her Master of Science degree in Materials Science and Engineering in December 2009, and her Doctor of Philosophy in Materials Science and Engineering May 2013.